Quaternary Science Reviews 197 (2018) 288–306

Contents lists available at ScienceDirect

Quaternary Science Reviews

journal homepage: www.elsevier.com/locate/quascirev

Rapid precipitation changes in the tropical West Pacific linked to North Atlantic climate forcing during the last deglaciation

Zhifang Xiong [a, b], Tiegang Li [a, b, *], Fengming Chang [c], Thomas J. Algeo [d, e], Peter D. Clift [f, g], Lisa Bretschneider [h], Zhengyao Lu [i], Xiao Zhu [c], Martin Frank [h], Peter E. Sauer [j], Fuqing Jiang [b, c], Shiming Wan [c], Xu Zhang [k], Shuangxi Chen [l], Jie Huang [c]

[a] Key Laboratory of Marine Sedimentology and Environmental Geology, First Institute of Oceanography, State Oceanic Administration, Qingdao 266061, China
[b] Laboratory for Marine Geology, Qingdao National Laboratory for Marine Science and Technology, Qingdao 266061, China
[c] Key Laboratory of Marine Geology and Environment, Institute of Oceanology, Chinese Academy of Sciences, Qingdao 266071, China
[d] Department of Geology, University of Cincinnati, Cincinnati, OH 45221-0013, USA
[e] State Key Laboratories of Biogeology and Environmental Geology, and Geological Processes and Mineral Resources, China University of Geosciences, Wuhan 430074, China
[f] Department of Geology and Geophysics and the Coastal Studies Institute, Louisiana State University, Baton Rouge, LA 70803, USA
[g] School of Geography Science, Nanjing Normal University, Nanjing 210023, China
[h] GEOMAR Helmholtz Centre for Ocean Research Kiel, Wischhofstrasse 1-3, 24148 Kiel, Germany
[i] Laboratory of Climate, Ocean and Atmosphere Studies, School of Physics, Peking University, Beijing 100871, China
[j] Department of Geological Sciences, Indiana University, Bloomington, IN 47405-1405, USA
[k] Alfred Wegener Institute Helmholtz Centre for Polar and Marine Research, Bussestrasse 24, D-27570 Bremerhaven, Germany
[l] Wuhan Center, China Geological Survey, Wuhan 430205, China

ARTICLE INFO

Article history:
Received 9 November 2017
Received in revised form
24 July 2018
Accepted 29 July 2018
Available online 29 August 2018

Keywords:
Chemical weathering
Terrigenous input
ITCZ
ENSO
AMOC
Western Philippine sea

ABSTRACT

The cause of rapid hydrological changes in the tropical West Pacific during the last deglaciation remains controversial. In order to test whether these changes were triggered by abrupt climate change events in the North Atlantic Ocean, variations in precipitation during the last deglaciation (18–10 ka) were extracted from proxy records of chemical weathering and terrigenous input in the western Philippine Sea (WPS). The evolution of chemical weathering and terrigenous input since 27 ka was reconstructed using the chemical index of alteration (CIA), elemental ratios (K/Al, TOC/TN and Ti/Ca), $\delta^{13}C_{org}$, terrigenous fraction abundance and flux data from International Marine Global Change Study Program (IMAGES) core MD06-3054 collected on the upper continental slope of eastern Luzon (northern Philippines). Sediment deposited during the Last Glacial Maximum (LGM) shows weathering equal to or slightly greater than Holocene sediment in the WPS. This unusual state of chemical weathering, which is inconsistent with lower air temperatures and decreased precipitation in Luzon during the LGM, may be due to reworking of poorly consolidated sediments on the eastern Luzon continental shelf during the LGM sea-level low-stand. Rapid changes in chemical weathering, characterized by higher intensity during the Heinrich event 1 (H1) and Younger Dryas (YD) and lower intensity during the Bølling-Allerød (B/A), were linked to rapid variations in precipitation in the WPS during the last deglaciation. The higher terrigenous inputs during the LGM relative to those of the Holocene were controlled by sea-level changes rather than precipitation. The terrigenous inputs show a long-term decline during the last deglaciation, punctuated by brief spikes during the H1 and YD related to sea-level rises and rapid precipitation changes in the WPS, respectively. The proxy records of chemical weathering and terrigenous input from eastern Luzon suggest high rainfall during the H1 and YD events, consistent with inferred rainfall patterns based on Fe/Ca records from offshore Mindanao. Rapid precipitation changes in the WPS did not coincide with migrations of the Intertropical Convergence Zone (ITCZ) but, rather, were related to state shifts of the El Niño-Southern Oscillation (ENSO) during the last deglaciation. Based on proxy records and modeling results, we argue that the Atlantic meridional overturning circulation (AMOC) controlled rapid

* Corresponding author. Key Laboratory of Marine Sedimentology and Environmental Geology, First Institute of Oceanography, State Oceanic Administration, Qingdao 266061, China.
E-mail address: tgli@fio.org.cn (T. Li).

https://doi.org/10.1016/j.quascirev.2018.07.040
0277-3791/© 2018 Elsevier Ltd. All rights reserved.

precipitation changes in the tropical West Pacific through zonal shifts of ENSO or meridional migration of the ITCZ during the last deglaciation. Our findings highlight the dominant role of the North Atlantic Ocean in the tropical hydrologic cycle during the last deglaciation.

© 2018 Elsevier Ltd. All rights reserved.

1. Introduction

Tropical hydrology influences global climate via the meridional Hadley and zonal Walker circulations and their teleconnections with extratropical climate features (Chiang, 2009). Precipitation, an important hydrological parameter, underwent abrupt changes in the tropical Pacific Ocean and on adjacent maritime continents during the last deglaciation (18–10 ka) (note: all ages are given in "ka", i.e., thousands of years before present). During the Heinrich event 1 (H1; 16.4–14.7 ka) and the Younger Dryas (YD; 12.7–11.6 ka), marine and terrestrial records from north of the equator show decreased precipitation (Wang et al., 2001; Partin et al., 2007; Saikku et al., 2009), whereas those from south of the equator show increased precipitation (Tachikawa et al., 2011; Denniston et al., 2013). This interhemispheric anti-phased rainfall pattern has been attributed to meridional shifts of the Intertropical Convergence Zone (ITCZ), with heavy southern rainfall and light northern rainfall associated with its southward migration during the H1 and YD (Gibbons et al., 2014; McGee et al., 2014). In addition, rainfall patterns during the last deglaciation were also influenced by mode shifts of the El Niño-Southern Oscillation (ENSO), with heavy rainfall in the eastern tropical Pacific and light rainfall in the western tropical Pacific linked to a persistent El Niño state during the H1 and YD (Stott et al., 2002). Thus, the meridional migration of the ITCZ and the zonal migration of the ENSO have been routinely invoked to account for changes in precipitation patterns in the tropical Pacific during the last deglaciation.

As more high-resolution millennial-scale climate records have been generated, it has become increasingly difficult to consistently apply the conventional mechanisms of ITCZ meridional migration and ENSO zonal migration to explain changes in tropical Pacific precipitation during the last deglaciation. First, some recently generated precipitation proxy records have departed from the interhemispheric anti-phased pattern. For example, decreased rainfall in the southern tropics during the H1 and YD was indicated by global ice volume-corrected surface seawater $\delta^{18}O$ ($\Delta\delta^{18}O_{sw\text{-}iv}$) records from offshore southern Indonesia (Gibbons et al., 2014), and increased rainfall in the northern tropics by X-ray fluorescence (XRF)-based Fe/Ca ratios for sediment cores from offshore Mindanao (Philippines) (Fraser et al., 2014). Second, the relative importance of the ITCZ versus ENSO as a control on precipitation changes in the tropical Pacific during the last deglaciation is still unclear. Some studies have invoked solely the ITCZ (Leduc et al., 2009) or ENSO as a control (Stott et al., 2002; Jia et al., 2015), whereas others have suggested that both were important controls on rainfall during the H1 and YD (Levi et al., 2007). Third, some tropical sites have failed to yield evidence of significant precipitation changes during the H1 or YD despite large inferred meridional displacements of the ITCZ (Partin et al., 2007). Similar difficulties for employing ITCZ and ENSO mechanisms to interpret precipitation patterns are encountered at not only millennial timescales but also orbital and centennial timescales. Kissel et al. (2010) found opposing trends in precipitation between land and marine areas, with weak rainfall in the western Philippine Sea (WPS) and strong rainfall in East Asia during higher boreal summer insolation. Yan et al. (2015) suggested that in-phase moisture changes in the equatorial West Pacific reflected contraction rather than meridional migration of the ITCZ during the Little Ice Age. The proposed mode of ITCZ expansion and contraction, which is based on observational data and proxy records of rainfall (Denniston et al., 2016; Wodzicki and Rapp, 2016), has been related to the meridional moist static energy gradient (Byrne and Schneider, 2016). The differing conclusions of these studies show that interpretation of precipitation patterns in the tropical Pacific at multiple timescales is still under debate.

The correspondence of precipitation changes in the tropical Pacific with the $\delta^{18}O$ record of the Greenland icesheet, and its implication that North Atlantic climate controlled tropical precipitation patterns during the last deglaciation, have been noted in many studies (e.g. Mohtadi et al., 2011; Denniston et al., 2013; Mollier-Vogel et al., 2013). This relationship has been attributed to a slowdown or shutdown of Atlantic meridional overturning circulation (AMOC), reducing northward oceanic heat transport and triggering a steepening of the interhemispheric sea surface temperature (SST) gradient during the H1 and YD (see review in Mohtadi et al., 2016). Variation in the interhemispheric SST gradient altered heat redistribution between the tropics and high-latitude Northern Hemisphere, thus directly influencing tropical precipitation during the last deglaciation (McGee et al., 2014). In this scenario, the mean meridional position of the ITCZ was sensitive to the interhemispheric SST gradient, with its southward shift corresponding to a weak AMOC (Broccoli et al., 2006; Chiang and Friedman, 2012). ENSO also responded to variations in AMOC, but its responsive behavior has been a matter of debate. Some studies have inferred that weakening of AMOC resulted in increased ENSO variability (Merkel et al., 2010) whereas others have inferred reduced ENSO variability (Timmermann et al., 2005). What is generally agreed is that ITCZ migration and ENSO mode shifts are a feedback or response of the climate system to changing AMOC strength. From this perspective, rapid precipitation changes in the tropical Pacific during the last deglaciation are likely to have been due to forcings emanating from the North Atlantic region.

Uncertainties in reconstructing precipitation patterns in the tropical Pacific during the last deglaciation are due in part to the nature of the employed proxies. To date, reconstruction of paleoprecipitation has been based mainly on two types of proxies: (1) $\Delta\delta^{18}O_{sw\text{-}iv}$ calculated from planktonic foraminiferal $\delta^{18}O$, and (2) proxies for sediment discharge related to freshwater runoff. Sometimes, these two types of proxies yield conflicting information regarding precipitation in the same marine area, and even in the same sediment core. For example, $\Delta\delta^{18}O_{sw\text{-}iv}$ data from three sediment cores in the WPS indicated decreased rainfall during the H1 and YD, but Fe/Ca records from one of the cores point to increased rainfall (Stott et al., 2002; Bolliet et al., 2011; Fraser et al., 2014). Such conflicts may be due to differences in the nature of these proxies: $\Delta\delta^{18}O_{sw\text{-}iv}$ reflects salinity variation in the ocean surface layer, thus integrating large-scale hydrological changes including not only rainfall but also evaporation and advection or upwelling of watermasses (Ravelo and Hillaire-Marcel, 2007; Fraser et al., 2014; Gibbons et al., 2014), whereas proxies for sediment discharge are sensitive only to local freshwater runoff and, thus, appear to be more robust and direct proxies for precipitation.

Precipitation plays a significant role in chemical weathering, transport, and delivery of terrigenous material from the continents to the ocean. Greater precipitation, along with higher air temperatures, generally enhances chemical weathering and bedrock erosion, increasing fluvial sediment fluxes (Kump et al., 2000; Clift, 2006; Gislason et al., 2009). Therefore, chemical weathering intensity and terrigenous sediment fluxes, as recorded in marine sedimentary successions, are considered to be viable proxies for precipitation in maritime continental areas. The Philippine archipelago consists mainly of andesitic-basaltic volcanic and sedimentary rocks, i.e., lithologies subject to intense chemical weathering in hot and humid climates, and it exhibits well-integrated drainage systems transporting sediment to the surrounding continental shelves. Modern chemical weathering processes in the Philippines have been studied using sediment and water samples from river basins and hot springs (Liu et al., 2009b; Schopka et al., 2011), but the chemical weathering history of this region since the late Quaternary has been not investigated to date. Modern and historical fluxes of terrigenous sediment from the Philippines to the South China Sea have been quantified (Liu et al., 2016), but a similar analysis of fluxes to the WPS has not been undertaken. In order to address these gaps, we reconstructed the long-term record of chemical weathering and terrigenous sediment flux changes to eastern Luzon since 27 ka using multiple geochemical proxies applied to the International Marine Global Change Study Program (IMAGES) core MD06-3054 (Fig. 1). In addition, we determined variability in precipitation in the WPS during the last deglaciation through analysis of chemical weathering and terrigenous flux data from the study core. These data and associated modeling results provide new insights regarding the origin of abrupt tropical hydrologic shifts in the western tropical Pacific during the last deglaciation.

2. Geological, climatic and oceanographic context

Luzon Island, located in the northern Philippines, is characterized by intra-arc strike-slip faulting, subduction, frequent seismicity, and active volcanism. The bedrock of Luzon consists of Cretaceous to Quaternary sedimentary and volcanic rocks and Cenozoic intermediate intrusive rocks (Liu et al., 2009b). The continental shelf along eastern Luzon is highly variable in width, ranging from several kilometers to more than two hundred kilometers (Fig. S1). Along much of its length, the adjacent continental slope is steep and furrowed by partly sediment-filled submarine canyons that act as conduits for movement of terrigenous sediments from coastal to offshore areas (Fig. S1a). These geomorphological relationships result in eustatic fluctuations exerting a strong influence on fluvial inputs from Luzon to the continental shelf and slope west of the East Luzon Trough and Philippine Trench, with generally higher fluxes associated with sea-level lowstands.

Precipitation over the Luzon region is controlled by seasonal meridional migration of the ITCZ and interannual zonal migration of ENSO. During the boreal winter (December to March), the wind direction is from the east to northeast (Fig. 2a) and rainfall is low (Fig. 2c, e), which is caused by the southward displacement of the ITCZ (Fig. 2c). During the boreal summer (June to September), the wind direction is from the west to southwest (Fig. 2b) and rainfall is high (Fig. 2d and e) related to the northward displacement of the ITCZ (Fig. 2d). The rainfall in the Luzon region shows pronounced seasonal variation due to the location of Luzon on the northern limit of the ITCZ (Fig. 2c and d), with an average of 2.2 mm/day in winter and 10.1 mm/day in summer (Fig. 2e). Rainfall in the WPS is also tightly coupled to ENSO events on interannual timescales (Fig. 2f and g). During El Niño years, rainfall is diminished due to the eastward shift of deep convection and precipitation cells over the Pacific (Lyon et al., 2006), whereas during La Niña years rainfall is enhanced by westward movement of these cells (Fig. 2f and g). The annual air temperature over the Luzon region varies only from 23.3 °C to 26.9 °C (average 25.3 °C), reflecting generally hot-warm conditions throughout the year (Fig. 2e).

Surface currents in the WPS are driven by the trade winds, with influences from bathymetric factors. The main surface current, the Pacific North Equatorial Current (NEC), flows from east to west at ~12–13 °N but splits into two branches as it approaches the eastern coast of the Philippines (Fig. 1; Qiu, 2001). The northern branch eventually forms the Kuroshio Current, whereas the southern branch gives rise to the Mindanao Current (Fig. 1).

3. Materials and methods

3.1. Sampling strategy

Core MD06-3054 was retrieved with a Calypso Giant Piston Corer on board *R/V* Marion Dufresne during the IMAGES XIV-MD155-Marco Polo 2 cruise in June 2006 (Laj and Shipboard Scientific Party, 2006). The coring site was located at 14°30.28′ N and 124°19.24′ E (Fig. 1), ~280 km offshore from the eastern coast of Luzon, Philippines (Fig. S1b). The core was recovered from a water depth of 2057 m, within a 35-km-wide basin on the upper continental slope. The 15.74-m-long core consists of an upper unit of homogenous gray silty clay (0–7.72 m) and a lower unit of olive gray clayey silt (7.72–15.74 m) containing turbidite layers at 9.45–9.50 m and 10.3–12.2 m. The turbidite layer at 9.45–9.50 m is characterized by sharp lower and upper contacts (Laj and Shipboard Scientific Party, 2006), a high abundance of coarse-fraction material (>63 μm; see Supplementary data), and a reversed AMS^{14}C age sequence (Fig. 3h). The core was initially sampled at 4-cm intervals for planktonic foraminiferal stable carbon and oxygen isotopes (Chen et al., 2011). In the present study, which required a high temporal resolution through the Last Glacial Maximum (LGM) and last deglaciation, samples were collected at intervals ranging from 2 to 32 cm through the uppermost 10.3 m of the core. Based on a *Globigerinoides ruber* δ^{18}O profile (Fig. 3b), the LGM, H1, Bølling-Allerød (B/A), and YD intervals were specifically targeted for AMS dating in order to generate an accurate timescale for these key events (Fig. 3h). A total of 122 samples were collected from core MD06-3054 (termed 'downcore samples'), ranging in age from 27 ka to the near-present with an average temporal resolution of ~220 yr per sample, which is sufficient to support oceanic and climatic interpretations on millennial time scales. To determine the concentrations of selected elements in the detrital fraction of modern bulk sediments from the WPS, one sample was obtained from near the top of each of three cores (termed 'core-top samples'), i.e., the study core (MD06-3054) plus cores MD06-3047B and MD06-3050 (Fig. 1).

3.2. AMS ^{14}C dating

Intact tests of the planktonic foraminifera *G. ruber* and *G. sacculifer* were handpicked from the 250–350-μm size fraction of 12 samples using a binocular microscope. Due to the low abundance of these two species in two samples, another subsurface-dwelling foraminiferal species (*Neogloboquadrina dutertrei*) was included yielding between 3 and 22 mg of material per sample for AMS ^{14}C dating (Table 1). Radiocarbon analysis was performed at the National Ocean Sciences Accelerator Mass Spectrometry (NOSMAS) facility in Woods Hole Oceanographic Institution (WHOI), USA, and an additional 4 samples were analyzed at Beta Analytic Corporation in Miami, USA. Radiocarbon ages were converted to calendar ages using

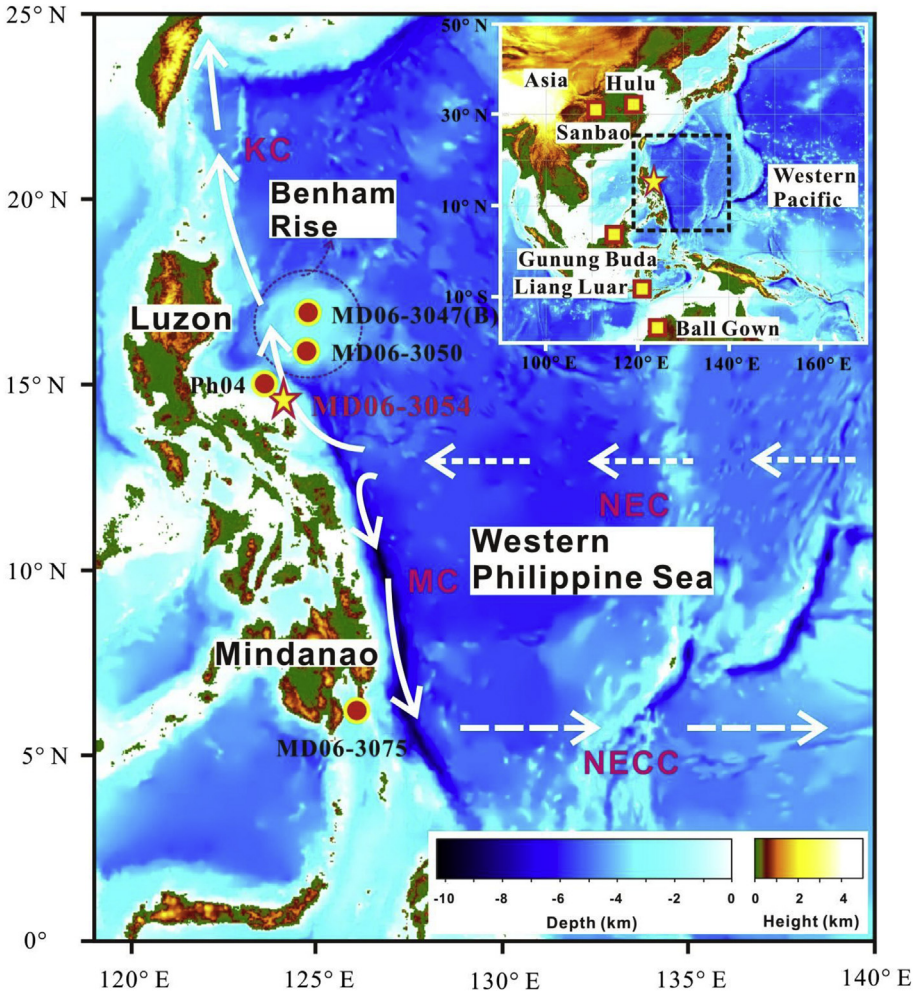

Fig. 1. Map of the WPS showing the locations of core MD06-3054, regional surface currents (modified from (Fine et al., 1994)), and the positions of selected cores discussed in this study (labeled symbols): MD06-3047B and MD06-3050 (this study), MD06-3047 (Xu et al., 2013), MD06-3075 (Fraser et al., 2014), and Ph04 (Jiang et al., 2013). Insert map of the tropical West Pacific showing the locations of core MD06-3054 (yellow star) and speleothem records from Hulu cave (Wang et al., 2001), Sanbao cave (Wang et al., 2008), Gunung Buda cave (Partin et al., 2007; Carolin et al., 2013), Liang Luar cave (Griffiths et al., 2009; Ayliffe et al., 2013), and Ball Gown cave (Denniston et al., 2013). Abbreviations: KC, Kuroshio Current; MC, Mindanao Current; NEC, North Equatorial Current; NECC, North Equatorial Counter Current. The general maps are drawn using gridview software of General Bathymetric Chart of the Oceans (GEBCO) (http://www.gebco.net/). (For interpretation of the references to colour in this figure legend, the reader is referred to the Web version of this article.)

the CALIB 7.0.2 program and updated Marine 13 calibration (Reimer et al., 2013), after applying a reservoir age correction of 480 years for samples younger than 13 ka, and 630 years for older samples. The adoption of these reservoir ages is consistent with practice in other recent studies of the WPS (Stott, 2007; Saikku et al., 2009; Bolliet et al., 2011; Fraser et al., 2014).

3.3. Geochemical analysis

Samples were freeze-dried and ground to a fine powder for geochemical analysis. An aliquot of each sample was analyzed for total carbon (TC) using an EA1112 HT Elemental Analyzer, with an analytical precision (RSD) better than 1.5%. A second aliquot was digested in 3-M HCl at room temperature overnight to remove carbonate, followed by decanting of residual acid, rinsing with deionized water, and centrifuging to remove chemical residues. The decalcified sample was freeze-dried and weighed before analysis of total organic carbon (TOC), total nitrogen (TN), and carbon isotopes of bulk organic matter ($\delta^{13}C_{org}$). TOC and TN measurements were performed on a Costech ECS4010 Elemental Analyzer with analytical precision (RSD) better than 1.4% and 1.8%, respectively. $\delta^{13}C_{org}$ was analyzed by oxidative elemental analyzer-isotope ratio mass spectrometry (EA-IRMS). The standards Acetanilide #1 ($\delta^{13}C = -29.53 \pm 0.01‰$) and EDTA-1 ($\delta^{13}C = -40.38 \pm 0.01‰$) were used to assess data quality yielding an analytical precision (SD) better than 0.08‰. Carbon isotopic results are reported in units of per mille (‰) variation relative to the Vienna Pee Dee Belemnite (VPDB) scale. $CaCO_3$ concentrations were calculated from TC and TOC data using the equation $\%CaCO_3 = 8.33 \times (\%TC - \%TOC)$ and assuming that all carbonate is calcite.

The three core-top samples were treated with 10% H_2O_2 at 60 °C for 4 h and then with 0.1-M HCl at room temperature for 24 h. These chemical pretreatments effectively removed most of the biogenic (i.e., carbonate and organic matter), authigenic (i.e., Fe-Mn oxides and phosphate), and adhered materials. This procedure did not remove biogenic silica, but its presence in the treated samples is unlikely to bias estimates of elemental concentrations in the detrital fraction because (1) the concentration of opal is low in the study core (1.6–4.8%; $n = 122$), and (2) our previous research showed that the concentrations of most elements (including major, trace, and rare earth elements) are not controlled by opal in diatom-rich sediments of the eastern Philippine Sea (Xiong et al.,

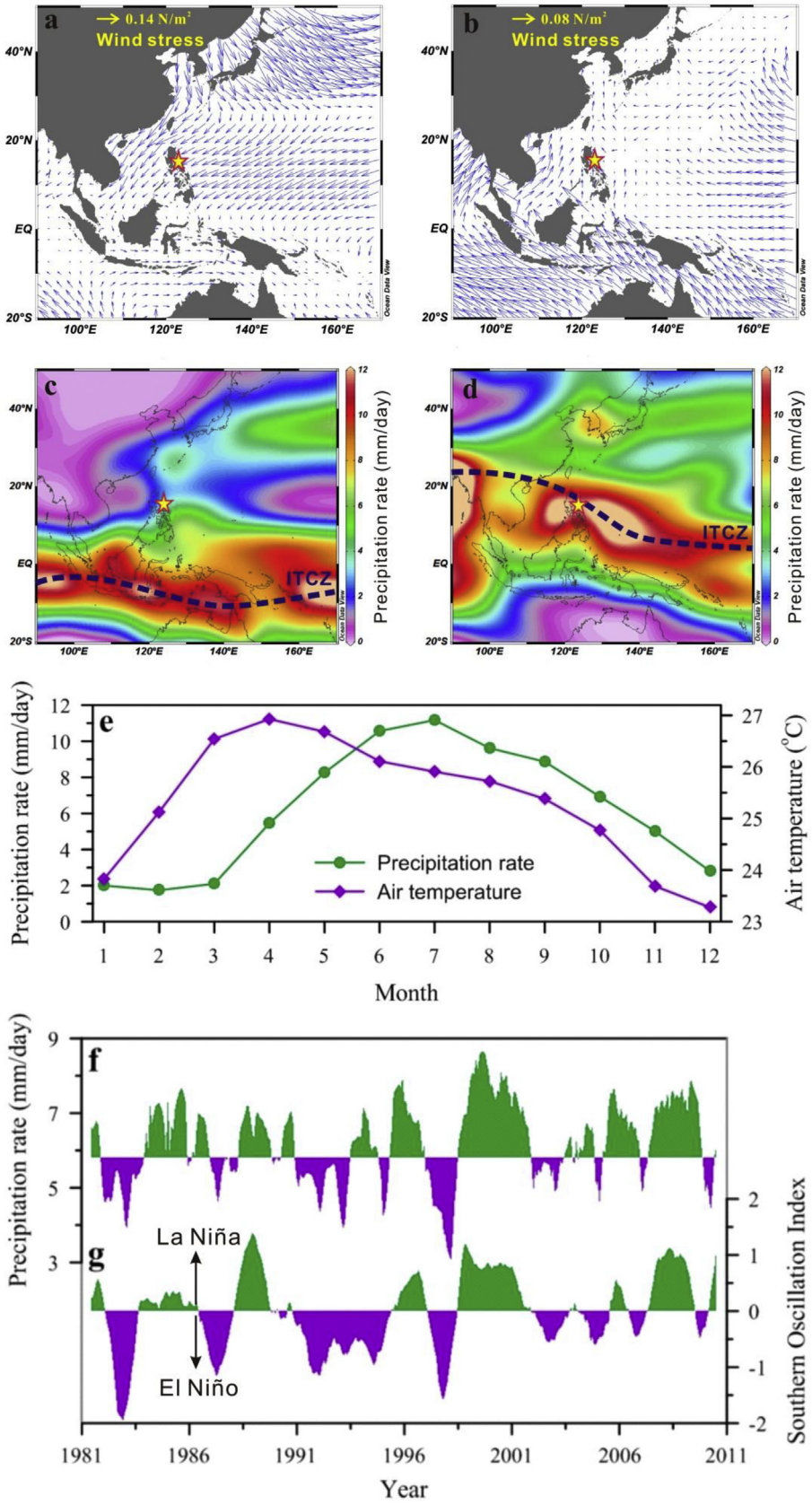

Fig. 2. The modern climatology of the tropical West Pacific. (a) and (b) Wind stress vector in January and July (2008). The wind stress data were obtained from http://giovanni.gsfc.nasa.gov. The yellow stars denote the location of MD06-3054. (c) and (d) Long term (1981–2010) mean precipitation rate in January and July. The yellow stars denote the location of MD06-3054. The blue dashed lines show the position of ITCZ. (e) Long term (1981–2010) monthly mean precipitation rate and air temperature in the study area (13–19 °N, 119.5–124.5 °E). The air temperature data are from http://www.esrl.noaa.gov/psd/data/gridded/data.UDel_AirT_Precip.html. (f) Monthly precipitation from 1981 to 2010 in the study area (13–19 °N, 119.5–124.5 °E) (11 point running average). In (c)–(f), the precipitation data were from http://www.esrl.noaa.gov/psd/data/gridded/data.cmap.html. (g) The Southern Oscillation Index (SOI) from 1981 to 2010 in the study area (13–19 °N, 119.5–124.5 °E) (11 point running average). The SOI data were obtained from http://iridl.ldeo.columbia.edu/SOURCES/.Indices/.soi. (For interpretation of the references to colour in this figure legend, the reader is referred to the Web version of this article.)

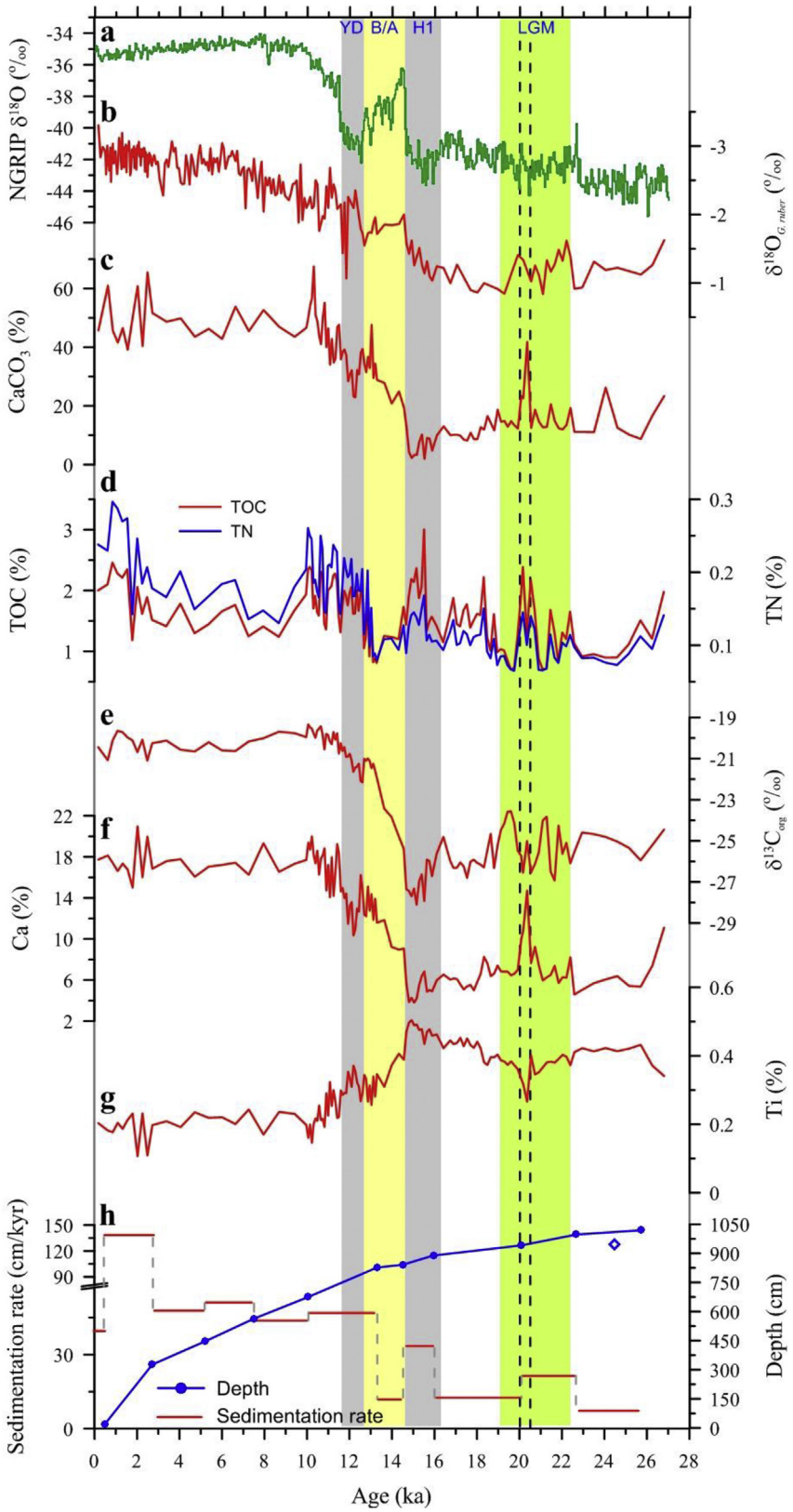

Fig. 3. Temporal variations of (a) NGRIP $\delta^{18}O$ (Andersen et al., 2004), and (b) $\delta^{18}O_{G.\ ruber}$ (Chen et al., 2011), (c) $CaCO_3$ content, (d) TOC and TN contents, (e) $\delta^{13}C_{org}$, (f) Ca concentration, (g) Ti concentration, and (h) sedimentation rate and age model in core MD06-3054. The reversed AMS ^{14}C age data (blue diamond) between 9.46 m and 9.48 m was not included in the age model. Green, gray, yellow bars indicate the LGM, H1 and YD, and B/A, respectively. The vertical double dashed lines mark the turbidite layer between 9.45 m and 9.50 m. (For interpretation of the references to colour in this figure legend, the reader is referred to the Web version of this article.)

Table 1
Planktonic foraminiferal AMS^{14}C dates and calibrated calendar ages for core MD06-3054.

Accession number	Depth (cm)	Materials	AMS^{14}C Age ± Error (yr B.P.)	2σ range of calendar age (yr B.P.)	Calendar age (yr B.P.)	Laboratory	Source
OS-72806	18–20	*G. ruber* and *G. sacculifer*	930 ± 30	429–523	481	WHOI	Chen et al. (2011)
OS-72709	326–328	*G. ruber* and *G. sacculifer*	3020 ± 30	2666–2781	2723	WHOI	Chen et al. (2011)
OS-72962	446–448	*G. ruber* and *G. sacculifer*	4980 ± 50	5027–5335	5218	WHOI	Chen et al. (2011)
OS-72965	562–564	*G. ruber* and *G. sacculifer*	7080 ± 35	7425–7560	7495	WHOI	Chen et al. (2011)
OS-72712	674–676	*G. ruber* and *G. sacculifer*	9320 ± 45	9902–10179	10060	WHOI	Chen et al. (2011)
OS-72808	826–828	*G. ruber* and *G. sacculifer*	11900 ± 45	13179–13405	13294	WHOI	Chen et al. (2011)
Beta-381861	840–842	*G. ruber*, *G. sacculifer* and *N. dutertrei*	12900 ± 40	14187–14819	14499	BETA	This study
Beta-381862	888–890	*G. ruber*, *G. sacculifer* and *N. dutertrei*	13900 ± 40	15786–16114	15948	BETA	This study
Beta-381863	940–942	*G. ruber* and *G. sacculifer*	17280 ± 50	19891–20274	20082	BETA	This study
OS-72713	946–948	*G. ruber* and *G. sacculifer*	21000 ± 90	24172–24859	24457	WHOI	This study
Beta-381864	996–998	*G. ruber* and *G. sacculifer*	19460 ± 60	22478–22899	22676	BETA	This study
OS-72803	1018–1020	*G. ruber* and *G. sacculifer*	22000 ± 85	25505–25890	25706	WHOI	Chen et al. (2011)

2012a; b). Leaching by dilute HCl does not result in a significant loss of detrital siliciclastic material (Wei et al., 2006), so the elemental composition of the post-leaching residuum was taken as representative of the detrital fraction of the bulk sediment.

Selected major and trace elements were measured in the whole-rock and detrital fractions of the three core-top samples (see above) as well as in the 122 whole-rock samples taken downcore from core MD06-3054. In preparation for elemental analysis, samples were dried at 50 °C and then ground to finer than 200 μm in an agate mortar. The concentrations of elements Ca, Ti, Al, K and Na were determined by conventional X-ray fluorescence on powder mounts using a PANalytical Axios Advanced PW4400 XRF. The concentrations of the elements La, Sc and Th were analyzed using a Thermo X-Series II Inductively Coupled Plasma-Mass Spectrometer (ICP-MS), in preparation for which an aliquot of sample powder was first digested with HF, HNO_3 and $HClO_4$, evaporated to dryness, and then dissolved in a fixed volume of aqua regia before addition of dilute HNO_3. For both procedures, analytical accuracy was assessed through analysis of selected Chinese national rock and sediment standards (GBW07103, GBW07104, GBW07108 and GBW07120), which gave results typically within ±5% of certified values for Ca, Ti, Al, K, Na and La, and within ±10% of certified values for Sc and Th. Analytical precision, given as the RSD, was determined by analyses of several duplicate samples and was typically better than 5% for major elements and La, and better than 10% for Sc and Th. The detection limits for Ca, Ti, Al, K, Na, La, Sc and Th were 0.036%, 0.001%, 0.053%, 0.041%, 0.037%, 1.0×10^{-6}, 1.0×10^{-6} and 1.0×10^{-6}, respectively.

Radiogenic Sr and Nd isotope compositions of the detrital fraction were measured on the core MD06-3054 and three core-top samples. The leaching procedures for extractions of the pure detrital fraction followed Jiang et al. (2013). Briefly, bulk dry samples were treated in separate steps with distilled and deionized water, acetic acid (10%), hydroxylamine hydrochloride (0.05 M), and hydrogen peroxide (5%) at room temperature to remove sea salts, carbonates, ferromanganese coatings, and organic matter, respectively. Residual detrital materials were then completely digested using alkaline fusion (NaOH-Na_2O_2), as described in Bayon et al. (2009), and further dissolved in 6 M HCl without addition of TiO_2, Fe_2O_3 or Tm. Standard column-chromatographic procedures were applied to separate and purify Sr and Nd (cf. Jiang et al., 2013). Sr and Nd isotope measurements were performed on a NuPlasma high-resolution multi-collector inductively coupled plasma-mass spectrometer (MC-ICPMS) at GEOMAR, Kiel, Germany. Measured Sr and Nd isotopic ratios were corrected for instrumental mass bias using $^{88}Sr/^{86}Sr$ of 0.1194 (Steiger and Jäger, 1977) and $^{146}Nd/^{144}Nd$ of 0.7129. Sr and Nd isotopic results were normalized to the accepted values of the JNdi-1 standard for Nd (0.512115; Tanaka et al., 2000) and of the NBS SRM 987 standard for Sr (0.710245) to account for instrument-specific offsets. The Nd isotopes were reported as $\varepsilon_{Nd}(0) = (((^{143}Nd/^{144}Nd)_{sample}/(^{143}Nd/^{144}Nd)_{CHUR} - 1) \times 10^4$, relative to the Chondritic Uniform Reservoir (CHUR) standard ($(^{143}Nd/^{144}Nd)_{CHUR} = 0.512638$; Jacobsen and Wasserburg, 1980). External reproducibilities (2σ) of Sr and Nd isotope measurements were ±0.0000267 and ± 0.5 $\varepsilon_{Nd}(0)$ units, respectively.

3.4. Paleoclimate modeling

In order to explore possible causes of rapid precipitation changes in the tropical West Pacific during the last deglaciation, we analyzed the baseline transient simulation (TRACE) conducted with the Community Climate System model version 3 (CCSM3). The atmosphere/land model resolution is ~3.75° (T31), and the ocean/sea-ice model has ~3.6° for zonal resolution with varying latitudinal resolution (~0.9° near the equator). The TRACE experiment is initialized from an equilibrium simulation forced by the LGM forcing, then integrated for 21,000 years, with transient boundary conditions including orbital parameters, greenhouse gas concentrations, continental icesheets, and meltwater fluxes. The long-term trend of mean climate (Shakun et al., 2012) as well as tropical climate variability (Liu et al., 2014) of TRACE experiments have been directly compared to available proxy records and show good agreement.

Our analysis focused on deglacial variability forced only by meltwater discharge (to perturb the AMOC; see Section 5.4), which was overlaid on the complete set of realistic climate forcings in TRACE simulations (Liu et al., 2014). We also show the results of the meltwater flux single-forcing experiment TRACE-MWF. In this simulation, we used the meltwater fluxes as the sole external forcing, while keeping other forcings at their LGM values to isolate the influence of AMOC response on climate variability. For more details of the model simulation, see He (2011) and Liu et al. (2014).

4. Results

4.1. Age model and sedimentation rates

The construction of an age model for the study core was based on linear interpolation of a set of 11 calibrated AMS^{14}C dates, excluding one anomalous date at 9.46–9.48 m (Table 1 and Fig. 3h). The 11 valid age data yielded a continuous sequence ranging between 25.71 ka and 0.48 ka. The single anomalous date (24.46 ka) is related to a turbidite layer at 9.45–9.50 m that was deposited during the LGM sea-level lowstand. Turbidite deposits dating to ~20–21 ka have also been reported from nearby cores MD06-3052 (Qiu et al., 2014) and MD98-2188 (Dang et al., 2009).

Our age model indicates that the upper 10.3 m of core MD06-3054 span the interval from 27 ka to the near-present. Overall, sedimentation rates gradually increased from the LGM through the last deglaciation to the Holocene. The Holocene is characterized by approximately constant sedimentation rates (~46 cm/kyr), except for extremely high sedimentation rates (~137 cm/kyr) from 2.72 to 0.48 ka. During the LGM and last deglaciation, sedimentation rates peaked at the LGM, H1 and YD, and fell to a minimum at the B/A (Fig. 3h).

4.2. Elemental and isotopic geochemistry

For downcore geochemical results, we were examining long-term trends that do take into consideration high-frequency variation during the deglaciation. $CaCO_3$ concentrations were relatively invariant during the LGM, increased gradually during the last deglaciation, and then stabilized at relatively high levels during the early and middle Holocene with some fluctuations in the late Holocene (Fig. 3c). The concentrations of Ti, Al, K, Na, La, Sc, and Th exhibit strong negative correlations with $CaCO_3$ and Ca (only Ti is shown in Fig. 3g; see Supplementary data for correlation coefficients), indicating that they are associated with the siliciclastic fraction and, thus, diluted by biogenic carbonate. The concentrations of TOC and TN show similar profiles, with a gradual increase (punctuated by a few fluctuations) during the LGM and last deglaciation and relatively low values in the early and middle Holocene (Fig. 3d). $\delta^{13}C_{org}$ exhibits a downcore trend similar to $CaCO_3$ concentration (Fig. 3e), pointing to the strong influence of marine carbonate production on organic carbon isotopic compositions. Also noteworthy is the superposition of rapid changes during the H1-B/A-YD interval on longer-term trends in many geochemical proxies (Fig. 3).

For the three core-top samples, the concentrations of Al, K, Sc and Th in the detrital fraction account for at least 72% of those in the whole-rock samples (Table 2), indicating that these elements reside dominantly in the detrital fraction. These findings are consistent with the results obtained from core MD06-3047 (Fig. 1), which suggest that most major elements (e.g., Al, Fe, Mg, K and P) have been concentrated in the detrital fraction over the past 700 kyr (Xu et al., 2013). Therefore, variation of these elements mainly resulted from processes related to detrital fluxes in core MD06-3054.

Unlike the geochemical proxies above, the Sr and Nd isotope signatures of the detrital fraction of core MD06-3054 show only a limited variability since the LGM. $^{87}Sr/^{86}Sr$ varied between 0.704324 and 0.706679, with an average value of 0.705308 (see Supplementary data; Fig. 4c). $\varepsilon_{Nd}(0)$ ranged from +3.05 to +5.22, with an average value of +4.28 (see Supplementary data). The Sr and Nd isotopic compositions of the detrital fraction in core MD06-3054 are almost identical to those of Luzon volcanic rocks (Defant et al., 1990), indicating detrital inputs mainly from Luzon with only minor contributions from Asian dust (Wu et al., 2010) (Fig. 4c).

5. Discussion

5.1. Sources of detrital fraction

The detrital fraction of Philippine Sea sediments is derived predominantly from weathering of volcanic rocks of the Philippine archipelago (mainly Luzon) with limited inputs of eolian dust from Asia (Wan et al., 2012; Xu et al., 2012; Jiang et al., 2013; Seo et al., 2014; Xiong et al., 2015). The relative contributions of weathered volcanic rocks versus eolian dust depend on the distance of a given depositional site from the Philippines and East Asia, seafloor topography, and climatic factors (e.g., precipitation, wind direction and shear). The proportion of Asian dust is greatest in distal offshore areas that receive limited riverine detritus and decreases with proximity to the Philippine archipelago. In the central and eastern Philippine Sea, the proportion of Asian dust in the detrital fraction ranges from ~50 to 90% (Seo et al., 2014; Xiong et al., 2015). On the Benham Rise in the WPS (i.e., east of the East Luzon Trough and Philippine Trench), the proportion of Asian dust falls to ~10–64% (Jiang et al., 2013, 2016; Xu et al., 2015), which is consistent with our new results (Fig. 4c). This proportion is yet lower on the Luzon continental shelf (i.e., west of the East Luzon Trough and Philippine Trench), e.g., <5% as estimated from radiogenic Sr-Nd isotopic data from core Ph04 (Fig. 4c; Jiang et al., 2013). The location of the present study core (MD06-3054) is proximal to that of core Ph04 (Fig. 1), suggesting that the detrital fraction of the sediment is dominated by weathering detritus from Luzon, with only limited contributions from Asian dust.

Other lines of evidence from core MD06-3054 support our inference that the detrital fraction is dominated by weathering materials from Luzon. First, in a La-Th-Sc discrimination diagram, both the core-top and downcore samples overlap largely with Philippine source rocks but not with Asian dust (Fig. 4a). Second, in an A-CN-K ternary diagram, both the core-top and downcore samples are located on the weathering trend for Luzon river

Table 2
Selected elemental composition of bulk and detrital fractions of three core-top samples from cores MD06-3047B, MD06-3050 and MD06-3054. The proportion of detrital materials in bulk sediments for every selected element was also estimated by the Ti-normalized calculations.

Core number	Interval (cm)	Fraction	Ti (%)	Al (%)	K (%)	Sc (10^{-6})	Th (10^{-6})	CIA
MD06-3047B	0–1	Bulk	0.39	7.43	0.98	20.83	2.44	54.7
		Detrital	0.55	9.51	1.15	29.16	4.18	69.1
		Detrital proportion[a]	1.00	0.89	0.82	0.98	1.19	
MD06-3050	8–10	Bulk	0.38	7.14	0.99	19.17	3.51	52.5
		Detrital	0.56	8.84	1.18	23.07	3.72	68.0
		Detrital proportion[a]	1.00	0.83	0.81	0.81	0.72	
MD06-3054	6–8	Bulk	0.24	4.30	0.50	10.31	1.24	46.5
		Detrital	0.55	9.41	0.91	22.26	2.83	71.5
		Detrital proportion[a]	1.00	0.94	0.78	0.93	0.98	

[a] $X_{Detrital\ proportion} = X_{Detrital} \times (Ti_{Bulk}/Ti_{Detrital})/X_{Bulk}$.

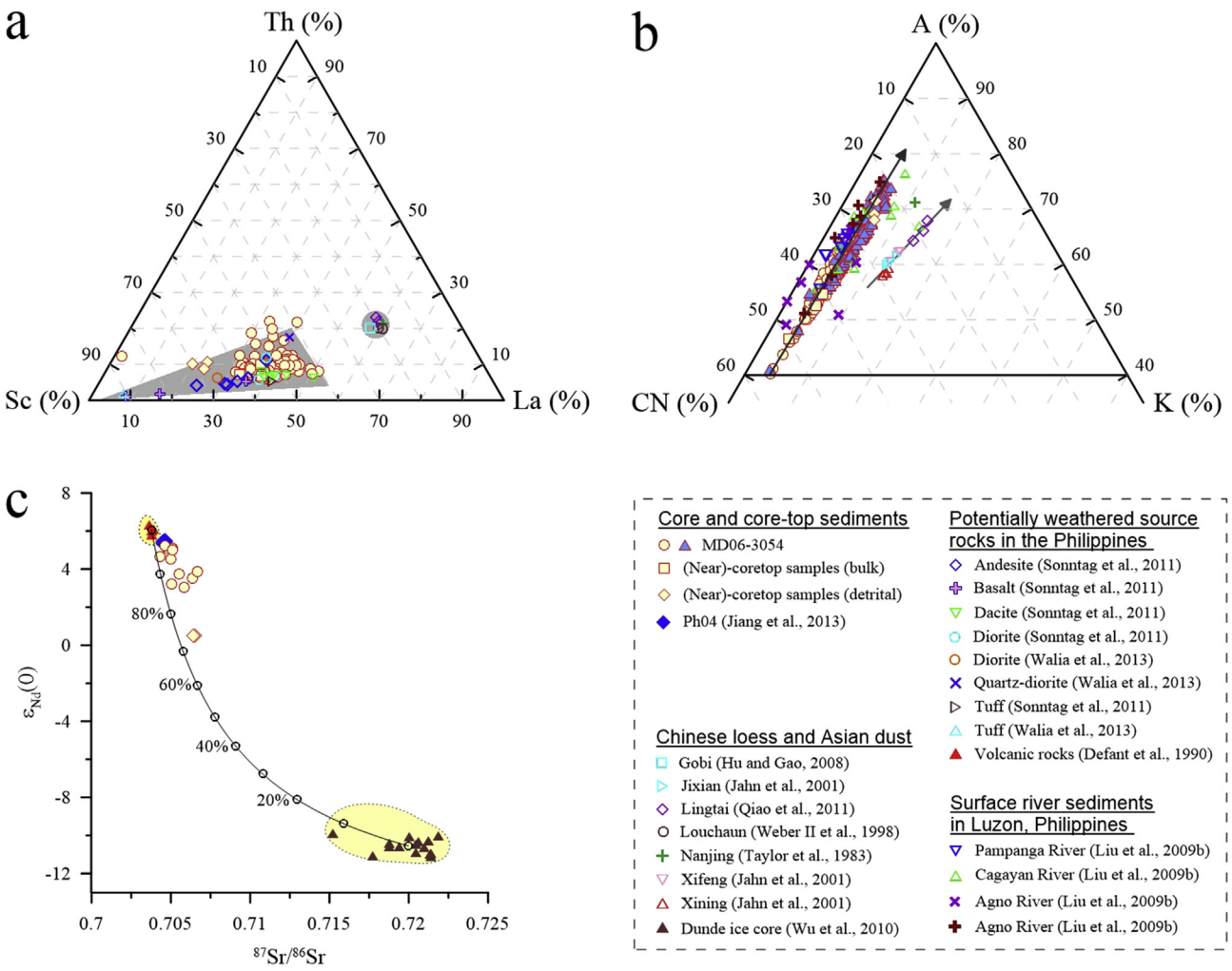

Fig. 4. Provenance discrimination of detrital materials in the study area. (a) La-Th-Sc ternary diagram, (b) A-CN-K ternary diagram, and (c) $^{87}Sr/^{86}Sr$-$\varepsilon_{Nd}(0)$ plot of detrital materials for core MD06-3054 and core-top samples. In (a), gray-shaded regions represent the La-Th-Sc composition ranges of Chinese loess and potentially weathered source rocks in the Philippines. In (b), $A = Al_2O_3$, $CN = CaO^* + Na_2O$, $K = K_2O$, all values are oxide molar concentrations; for the definition and calculation of CaO^*, please refer to Section 5.2.1. The arrows show the weathering trends of Chinese loess and surface river sediments in Luzon, Philippines. In (c), the solid line is the mixing curve between two potential source areas (marked by yellow shaded regions), which is developed from average concentrations and isotopes of Sr and Nd of volcanic rocks from Luzon (Sr = 439.5 ppm, Nd = 19.1 ppm, $^{87}Sr/^{86}Sr = 0.703775$ and $^{143}Nd/^{144}Nd = 0.512949$ ($\varepsilon_{Nd}(0) = 6.1$); Defant et al., 1990) and Asian dust from the Dunde ice core, northern China (Sr = 143.8 ppm, Nd = 27.8 ppm, $^{87}Sr/^{86}Sr = 0.719982$ and $^{143}Nd/^{144}Nd = 0.512097$ ($\varepsilon_{Nd}(0) = -10.6$); Wu et al., 2010). The relative percentages of volcanic material are marked with circles on the line, with each point indicating 10%. $^{87}Sr/^{86}Sr$ and $\varepsilon_{Nd}(0)$ of detrital fraction from core Ph04 are adopted from Jiang et al. (2013). Other data sources: Taylor et al., 1983; Weber II et al., 1998; Jahn et al., 2001; Hu and Gao, 2008; Liu et al., 2009b; Qiao et al., 2011; Sonntag et al., 2011; Walia et al., 2013. (For interpretation of the references to colour in this figure legend, the reader is referred to the Web version of this article.)

sediments rather than that for Asian dust (Fig. 4b). Finally, down-core samples are close to the mixing curve between the two potential endmember sources (i.e., Luzon volcanic materials and Asian dust) in the $^{87}Sr/^{86}Sr$-$\varepsilon_{Nd}(0)$ plot (Fig. 4c). Quantitative calculations based on the $\varepsilon_{Nd}(0)$ data show that weathering detritus from Luzon contributed 87–96% (average 92%) of the detrital material in the study core (Fig. 4c). These estimates are consistent with the results obtained from nearby core Ph04 in the study area (Jiang et al., 2013). These observations imply that the detrital fraction of the study core was derived mainly from weathering of rocks on the Philippine archipelago.

5.2. Climatic-oceanographic controls on chemical weathering in Luzon

5.2.1. Chemical weathering proxies

The degree of chemical weathering of the detrital silicate fraction of marine sediments can be estimated using the chemical index of alteration (CIA), with higher CIA values reflecting more intense chemical weathering (Nesbitt and Young, 1982; Price and Velbel, 2003). CIA is defined as:

$$CIA = Al_2O_3 / (Al_2O_3 + CaO^* + Na_2O + K_2O) \times 100 \quad (1)$$

where all values are oxide molar concentrations. CaO^* represents the CaO content of the silicate fraction, which is used in place of total CaO in order to avoid contributions from the carbonate and phosphate fractions. We calculated CaO^* using two methods. In the first method (McLennan, 1993), we determined the CaO/Na_2O molar ratio of the bulk sediment and substituted Na_2O for CaO^* when CaO/Na_2O was >1.0 but used measured CaO as CaO^* when CaO/Na_2O was <1.0. In the second method, CaO^* was calculated by subtracting carbonate CaO from total CaO, i.e., $CaO^* = CaO - 4.67 \times TIC$, where TIC = TC – TOC (total inorganic carbon is equal to total carbon minus total organic carbon). The second procedure assumes that all carbonate in the study samples is calcite and that

phosphate-Ca is negligible; these assumptions are reasonable for the study samples because Mg, Fe, and Mn concentrations are typical of detrital siliciclastics (thus excluding significant quantities of non-calcite carbonates) and P concentrations are low (~0.07–0.13%).

The two methods yielded quite similar CIA trends except within the interval from 20 to 15 ka, where the CIA values based on the CaO/Na_2O method show a small rise but those estimated by the TIC method show a weak decline (Fig. 5b). However, the two methods yield different absolute CIA values through the full study interval, with those based on the CaO/Na_2O method being generally lower (range 40.2–64.2, mean 57.2) than those based on the TIC method (range 40.7–75.1, mean 63.9) (Fig. 5b). This difference may indicate that the CaO/Na_2O method tends to underestimate CIA values, as proposed by Shao and Yang (2012). The higher absolute values yielded by the TIC method appear to be more compatible with the tropical climate of Luzon. However, the long-term trend of the CIA profile based on the CaO/Na_2O method matches that of another chemical weathering proxy (i.e., K/Al; see below) better than the trend of the TIC method, especially for the 20–15 ka interval. These observations suggest that CIA estimation methods for bulk sediments have shortcomings relative to direct calculation of CIA for acid-leached bulk sediments. Consequently, we will use only the CIA profile yielded by the CaO/Na_2O method for discussion of paleoceanographic implications owing to its greater consistency with K/Al (see Section 5.2.2).

The CIA values indicate low to moderate weathering intensity of detrital materials in the study core (Fig. 5b), based on the definitions of weak (CIA = 50–60), moderate (CIA = 60–80), and strong chemical weathering (CIA >80) of Fedo et al. (1995). Modern river sediments on Luzon also yield CIA values reflecting low to moderate chemical weathering (Liu et al., 2009b), which is supported by the CIA values of the bulk and detrital fractions of the core-top samples of this study (Table 2). These results suggest that Luzon has not experienced strong chemical weathering during the last 27 kyr, a finding that appears inconsistent with a tropical climate marked by warm temperatures and heavy rainfall. This anomaly has been observed previously and has been explained by a weathering-limited regime characterized by high denudation rates (West, 2012), i.e., physical weathering of freshly exposed rock happens so quickly that the eroded material does not have time to be strongly weathered chemically.

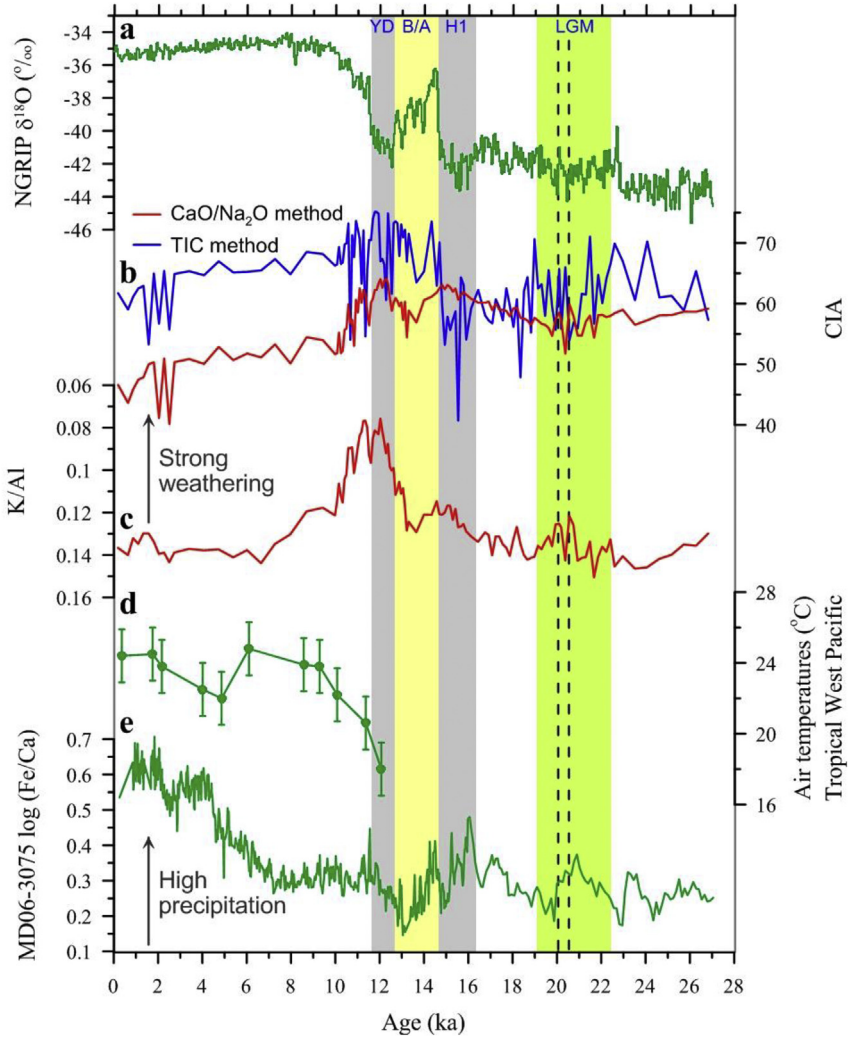

Fig. 5. Temporal variations of (a) NGRIP $\delta^{18}O$ (Andersen et al., 2004), and (b) CIA, (c) K/Al in core MD06-3054, and (d) air temperatures over tropical West Pacific derived from $\delta^{18}O$ of speleothem calcite and fluid inclusions in Liang Luar cave, southern Indonesia (Griffiths et al., 2010), and (e) XRF core scanning record of log(Fe/Ca) in core MD06-3075 (Fraser et al., 2014). Note that the K/Al scale is inverted, the purpose of which is to show stronger chemical weathering as upward trends. Green, gray, yellow bars indicate the LGM, H1 and YD, and B/A, respectively. The vertical double dashed lines mark the turbidite layer between 9.45 m and 9.50 m. (For interpretation of the references to colour in this figure legend, the reader is referred to the Web version of this article.)

The basis for use of K/Al as a chemical weathering proxy is the same as that for CIA, i.e., mobile elements such as K and Na are easily leached but immobile elements such as Al and Ti tend to be concentrated in the residue during chemical weathering (Hu et al., 2013; Lupker et al., 2013; Clift et al., 2014). Although K can also be enriched in weathering products, this process occurs after moderate chemical weathering (Nesbitt et al., 1980; Nesbitt and Markovics, 1997). CIA values indicate low to moderate weathering intensity for detrital materials, implying that K was easily leached off weathering profiles for the study core (Fig. 5b). Therefore, low K/Al ratios point to relatively strong chemical weathering (Fig. 5c).

5.2.2. Chemical weathering linked to temperature and precipitation

The weathering proxies used in this study do not show a consistent relationship of chemical weathering intensity to temperature during the Late Quaternary. Although CaO/Na_2O-based CIA suggests more intense chemical weathering for the LGM (mean 56.7) than for the Holocene (mean 49.3; Fig. 5b), the other two weathering proxies yield similar values for the LGM (TIC-based CIA = 61.2; K/Al = 0.135) and the Holocene (TIC-based CIA = 63.5; K/Al = 0.134; Fig. 5b and c). Furthermore, the weathering proxies appear to record more intense chemical weathering during colder intervals relative to warmer intervals of the Late Quaternary. For example, within the interval of high-frequency climate change during the last deglaciation, the cold H1 and YD events are characterized by higher CIA and lower K/Al (more intense weathering) and the warm B/A event by lower CIA and higher K/Al (less intense weathering) (Fig. 5b and c).

A climatic control on the chemical weathering changes observed in core MD06-3054 can be evaluated through comparison with contemporaneous climatic and oceanographic records from the WPS. As revealed by model, laboratory and field studies, temperature and moisture are the two dominant factors that control the intensity of chemical weathering, with high temperature and heavy rainfall enhancing silicate weathering (White and Blum, 1995; Kump et al., 2000; West et al., 2005; Gislason et al., 2009). Air temperature records over the WPS since the LGM are unavailable at present, although a continuous record since 12 ka is available from speleothem fluid inclusions in southern Indonesia (Fig. 1). This record shows a ~5 °C cooling during the YD compared to the present day and relatively stable temperatures of ~24 °C during the Holocene (Fig. 5d) (Griffiths et al., 2010). The result is in good agreement with air temperature reconstructed from the $\delta^{18}O$ records of ice cores from high-elevation tropical sites (Thompson et al., 1995, 1998) and from Greenland (Andersen et al., 2004), suggesting that tropical West Pacific air temperature can be proxied by these records (Fig. 5a). On the other hand, precipitation is invariably influenced by local factors, so far-field records are not suitable proxies (Mohtadi et al., 2016). For this reason, we made use of a proxy record based on XRF-derived log(Fe/Ca) ratios from the MD06-3075 core located offshore of Mindanao in the southern Philippines (Fraser et al., 2014) as a proxy for precipitation on Luzon since the LGM (Fig. 5e). These climate proxy records demonstrate that air temperatures and precipitation levels on Luzon were reduced during the LGM relative to the Holocene (Fig. 5a, e) (Andersen et al., 2004; Fraser et al., 2014). This pattern should have led to weaker chemical weathering during the LGM, but the weathering indices used in this study suggest that weathering intensity during the LGM was equal to or greater than that of the Holocene (see above; Fig. 5b and c).

The alternative to climatic control of weathering proxies is that changes in sediment dispersal during the LGM resulted in inputs of more highly weathered material to the eastern Luzon Shelf. One likely mechanism is reworking of older shelf sediments as a result of sea-level fall (Hu et al., 2013, 2016; Dou et al., 2016). Sea level is estimated to have fallen ~110–125 m in the West Pacific region during the LGM (Fig. 6f) (Yokoyama et al., 2000; Liu et al., 2004), exposing the continental shelf up to ~250 km offshore from the modern Luzon coastline (Fig. S1b, c). Rivers eroded upper-shelf sediments and transported the material to the study site via canyons on the lower continental shelf and upper continental slope (Fig. S1a). The reworked material may represent sediments that were subaerially weathered and deposited on the eastern Luzon Shelf during the last (Sangamon) interglacial, which was characterized by high temperatures and heavy rainfall in the WPS region (Bolliet et al., 2011; Fraser et al., 2014). The rapidity of shifts in weathering proxies during the LGM is probably more consistent with changes in sediment remobilization and transport than in short-term climate variation. The 'reworking hypothesis' has been invoked previously to explain the deposition of strongly weathered sediment during the LGM on continental shelves in the South China Sea, the Arabian Sea, and the Southern Ocean (Latimer and Filippelli, 2001; Boulay et al., 2007; Limmer et al., 2012).

The more weathered condition of sediment deposited during the H1 and YD was probably not due to reworking of eastern Luzon Shelf sediments during the last deglaciation. Unlike the LGM, the last deglaciation was characterized by a continuous rise in sea level that was mostly gradual but punctuated by two rapid rises associated with meltwater pulse (MWP-) 1A at 14.6–14.3 ka and MWP-1B at 11.4–11.1 ka (Hanebuth et al., 2000; Liu et al., 2004; Bard et al., 2010) (Fig. 6f). Rising sea levels reduced the area of emergent shelf, thus limiting reworking of older sediments. Although several studies have inferred that shelf currents can rework older deposits (e.g., Steinke et al., 2008), there is at present no evidence for such a mechanism in the WPS during the last deglaciation. We infer that the more intensely weathered sediment deposited during the last deglaciation reflects contemporaneous climate conditions on Luzon. However, stronger chemical weathering during H1 and YD, and weaker weathering during B/A, cannot be ascribed to a temperature control, because temperatures were low during H1and YD and high during B/A (Fig. 5b–d). On the other hand, variation in chemical weathering intensity matches inferred changes in rainfall levels during the last deglaciation, with higher weathering intensity correlating with heavy rainfall during the H1 and YD, and diminished weathering intensity correlating with weaker rainfall during the B/A (Fig. 5b, c and e). Therefore, we infer that precipitation rather than temperature was the dominant control on chemical weathering in Luzon during the last deglaciation.

For all geologically young sedimentary records, an important question is the degree to which human activity has influenced them. Luzon was first settled by humans at ca. 67 ka (Mijares et al., 2010), and agriculture first appeared at ca. 10 ka (i.e., Neolithic period; Stevenson et al., 2010, and references therein) and intensified with rising human populations after ca. 4.5–3.0 ka (Bellwood and Dizon, 2013). These dates, although based on limited data, are sufficient to suggest that human activity on Luzon possibly has had an effect on sediment fluxes since the early Holocene and almost certainly during the late Holocene. However, quantitative studies of the magnitude of the anthropogenic effect on riverine sediment fluxes on Luzon have not been undertaken to date. In view of the likelihood of anthropogenic influences on the Holocene part of core MD06-3054, we will not attempt to infer climatic-oceanographic controls on chemical weathering and terrigenous input proxies since 10 ka.

5.3. Climatic-oceanographic controls on terrigenous inputs to offshore Luzon

5.3.1. Terrigenous input proxies

Organic matter in marine sediments is composed of a mixture of

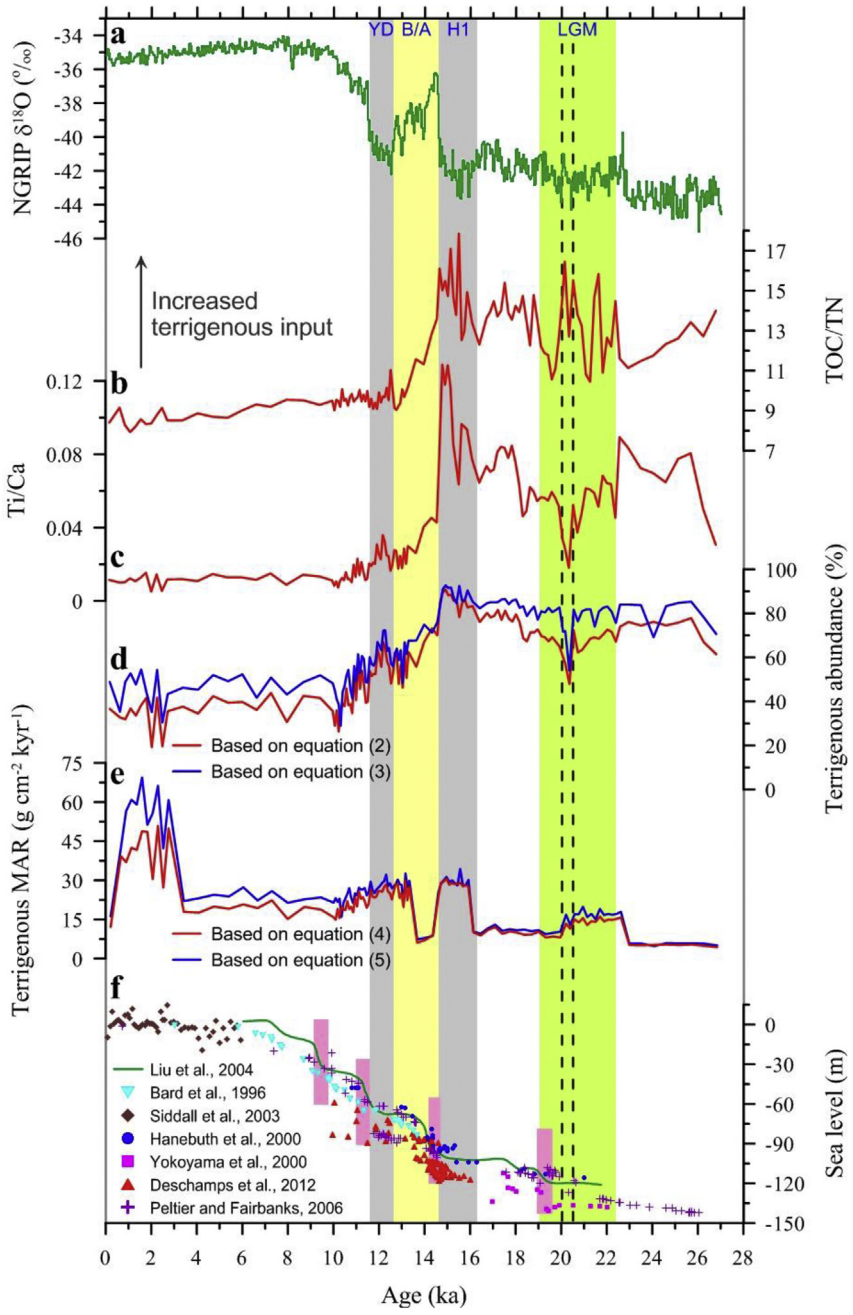

Fig. 6. Temporal variations of (a) NGRIP $\delta^{18}O$ (Andersen et al., 2004), and (b) TOC/TN, (c) Ti/Ca, (d) terrigenous abundance, (e) terrigenous MAR in core MD06-3054, and (f) global sea level fluctuations. In (f), four pink bands mark the 19-ka MWP, MWP-1A, MWP-1B and MWP-1C (Hanebuth et al., 2000; Clark et al., 2004; Liu et al., 2004; Bard et al., 2010; Deschamps et al., 2012). Green, gray, yellow bars indicate the LGM, H1 and YD, and B/A, respectively. The vertical double dashed lines mark the turbidite layer between 9.45 m and 9.50 m. Other Data sources for (f): Bard et al., 1996; Yokoyama et al., 2000; Siddall et al., 2003; Peltier and Fairbanks, 2006. (For interpretation of the references to colour in this figure legend, the reader is referred to the Web version of this article.)

autochthonous marine and allochthonous terrigenous organic matter. Owing to differences in composition, the relative amounts of organic matter derived from each source can be estimated from TOC/TN and $\delta^{13}C_{org}$ data by assuming a fixed characteristic composition for each endmember. However, such calculations are complicated by the presence of ^{13}C-enriched C4 plant material and by changes in composition related to organic matter decay. In a general sense, higher TOC/TN and lower $\delta^{13}C_{org}$ point to increased inputs of terrigenous organic matter to the study site (see Supplementary Information).

Our inferences regarding the time-dependency of organic matter sources can be compared with proxies for terrigenous inputs to the study site. Ti/Ca represents a measure of the relative fluxes of terrigenous detritus to biogenic carbonate (Tachikawa et al., 2011; Chang et al., 2015). The study core is well above the modern lysocline (~3400 m), i.e., at depths at which carbonate dissolution is expected to be negligible (Berger et al., 1982; Groetsch et al., 1991), so carbonate preservation state is unlikely to have influenced Ti/Ca ratios. The importance of terrigenous inputs can be quantitatively estimated in terms of terrigenous abundance (TA) and terrigenous mass accumulation rate (TMAR), each of which can be calculated by two different methods. First, TA can be

calculated from the Ti concentration of the bulk sediments assuming that all Ti is of terrigenous origin (Schroeder et al., 1997):

$$TA = (Ti_{sample} / Ti_{detrital}) \times 100\% \quad (2)$$

where Ti_{sample} and $Ti_{detrital}$ denote the Ti concentrations of samples and the detrital background of the study area. For TA calculations, estimation of $Ti_{detrital}$ is the critical variable, especially since continent-margin sediments can have a compositionally variable terrigenous fraction (Reitz et al., 2004). Here, we estimate $Ti_{detrital}$ from the detrital fraction of the three core-top samples in the WPS (0.55%) (Table 2), which is close to the average Ti concentration of river sediments in eastern Luzon (0.48%) (Liu et al., 2009b). Second, TA can be calculated by considering the bulk sediment to be composed exclusively of terrigenous and biogenic ($CaCO_3$, TOC, and opal) fractions (Riethdorf et al., 2013):

$$TA = 100\% - (CaCO_3 + TOC + opal) \quad (3)$$

In this calculation, TN is not included due to its low concentration (<0.3%; Fig. 3d), and marine organic carbon is not excluded in view of the low concentrations of TOC (<3.1%; Fig. 3d). Accordingly, TMAR can be calculated by either of two equations:

$$TMAR = (Ti_{sample} / Ti_{detrital}) \times R \times D \quad (4)$$

$$TMAR = [1 - (CaCO_3 + TOC + opal)] \times R \times D \quad (5)$$

where R and D are linear sedimentation rate and dry bulk sediment density, respectively. The two methods yield nearly identical downcore trends for TA and TMAR in the study core (Fig. 6d and e). These trends indicate that the proportion of terrigenous material input to the study site decreased markedly from ~70 to 90% to ~40–60% during the last deglaciation. This is consistent with increased trapping of terrigenous siliciclastics in nearshore areas during the deglacial eustatic transgression (Swift and Thorne, 1991). We note that TMAR does not show a long-term trend like other terrigenous input proxies (i.e., TOC/TN, $\delta^{13}C_{org}$, Ti/Ca, and TA). Further, TMAR exhibits an obvious peak at 2.8–0.5 ka whereas other terrigenous input proxies do not. These inconsistences resulted from the adoption of sedimentation rate in the calculation of TMAR. Sedimentation rate represents an average over a period of time and not the instantaneous rate of sediment accumulation, thus detrending the variation itself. The sedimentation rate also shows a peak during the 2.8–0.5 ka interval and, thus, the TMAR value is dominated by the sedimentation rate. However, other terrigenous input proxies were not influenced by sedimentation rate. The anomalously high TMAR and sedimentation rates during the 2.8–0.5 ka interval were thus probably caused by increased human activity during the late Holocene (see Section 5.2.2).

5.3.2. Terrigenous inputs linked to sea level and precipitation

The record of the last deglaciation in our core is characterized by rapid fluctuations followed by pronounced shifts in TOC/TN, $\delta^{13}C_{org}$ and Ti/Ca (Figs. 3e and 6b, c), as well as in the calculated parameters TA and TMAR (Fig. 6d and e). Collectively, these proxies indicate that terrigenous inputs to the Luzon Shelf declined gradually following the LGM, although this decline was interrupted by rapid changes during the last deglaciation. Specifically, terrigenous inputs increased sharply during H1, decreased abruptly during the B/A, and then increased modestly during the YD, reflecting a close relationship to global climate shifts. Greater terrigenous inputs during the LGM, H1, and YD are associated with higher sedimentation rates (Figs. 3e, h and 6b-e).

The supply of terrigenous materials to marginal seas is generally controlled by sea level, precipitation, and fluvial transport, which are interrelated factors (Martinez et al., 2007; Govin et al., 2014; Zhang et al., 2015). Seafloor bathymetry and ocean currents can influence the dispersal of terrigenous sediments but do not influence their rate of delivery or degree of weathering (Arz et al., 1999). In the WPS region, oceanward transport of terrigenous sediments is constrained by the East Luzon Trough and Philippine Trench as well as the northwestward-flowing Kuroshio Current (Fig. 1), contributing to their trapping on the continental shelf and slope of eastern Luzon. During the LGM when sea-level was ~110–125 m lower than at present (Fig. 6f) (Yokoyama et al., 2000; Liu et al., 2004), the study site was located more proximally to the eastern Luzon coastline and its river mouths (Fig. S1). These conditions favored transport of terrigenous sediments to the outer Luzon Shelf even though rainfall on Luzon was low during the LGM (Fig. 5e). Moreover, reworking and transport of exposed older inner-shelf sediments also may have contributed to increased terrigenous inputs to the outer Luzon Shelf during the LGM (see Section 5.2.2).

During the last deglaciation as sea level rose from ~105 to 35 m below the modern level, rainfall did not experience a simple long-term trend but, instead, was characterized by rapid variation (Figs. 5e and 6f). The gradual rise of sea level was paralleled by a long-term decline in terrigenous inputs at that time, supporting an inference of dominant control of terrigenous fluxes by sea-level elevation. More rapid changes occurred in conjunction with the transition from H1 to B/A, which roughly corresponds to MWP-1A, during which sea level rose ~16 m in ~300 years (14.6–14.3 ka) (Hanebuth et al., 2000; Deschamps et al., 2012). At that time, TOC/TN, $\delta^{13}C_{org}$ and Ti/Ca fell sharply, reflecting a rapid decline in terrigenous inputs (Figs. 3e and 6b, c). During this transition, TA decreased from ~90 to 70% and TMAR decreased from ~30 to 10 g cm^{-2} kyr^{-1} (Fig. 6d and e). The sharp decline in terrigenous inputs to the outer Luzon Shelf during this interval was probably due to trapping of terrigenous siliciclastics in inner-shelf areas.

Sea-level change can explain the long-term variation in terrigenous inputs to the outer Luzon Shelf since the LGM, but it cannot account for large fluctuations in terrigenous fluxes during the last deglaciation, when sea level continued to rise unabated. The last deglaciation was punctuated by three meltwater pulses (MWP-1A, MWP-1B and MWP-1C) that caused rapid sea-level rises (Hanebuth et al., 2000; Liu et al., 2004; Bard et al., 2010; Deschamps et al., 2012), but only MWP-1A shows a response in terrigenous flux records. In fact, terrigenous fluxes during H1 exceeded those of the LGM, a pattern that cannot have been caused by rising sea-level elevations. Therefore, we invoke changes in precipitation to explain rapid changes in terrigenous inputs during the last deglaciation. Available precipitation proxies indicate that higher rainfall was associated with the H1 and YD, and lower rainfall with the B/A (Fig. 5e) (Fraser et al., 2014).

5.4. Precipitation variability in the WPS during the last deglaciation

Both chemical weathering and terrigenous input proxies indicate rapid precipitation changes in the Luzon region during the last deglaciation (Fig. 7b). Combined with rainfall records from offshore Mindanao (Fraser et al., 2014) (Fig. 7c), they suggest that the WPS underwent rapid precipitation changes with high levels during the H1 and YD, and low levels during the B/A. However, these results based on terrigenous proxies are in conflict with those from marine indicators in the WPS. Specifically, cores MD98-2181 and MD06-3067 show high $\Delta\delta^{18}O_{sw\text{-}iv}$ (a seawater salinity proxy) during the H1 and/or YD, implying lower rainfall in the WPS region during those stages (Stott et al., 2002; Saikku et al., 2009; Bolliet et al., 2011). The $\Delta\delta^{18}O_{sw\text{-}iv}$ and log(Fe/Ca) proxies from core MD06-3075 thus yield opposing interpretations with respect to rainfall

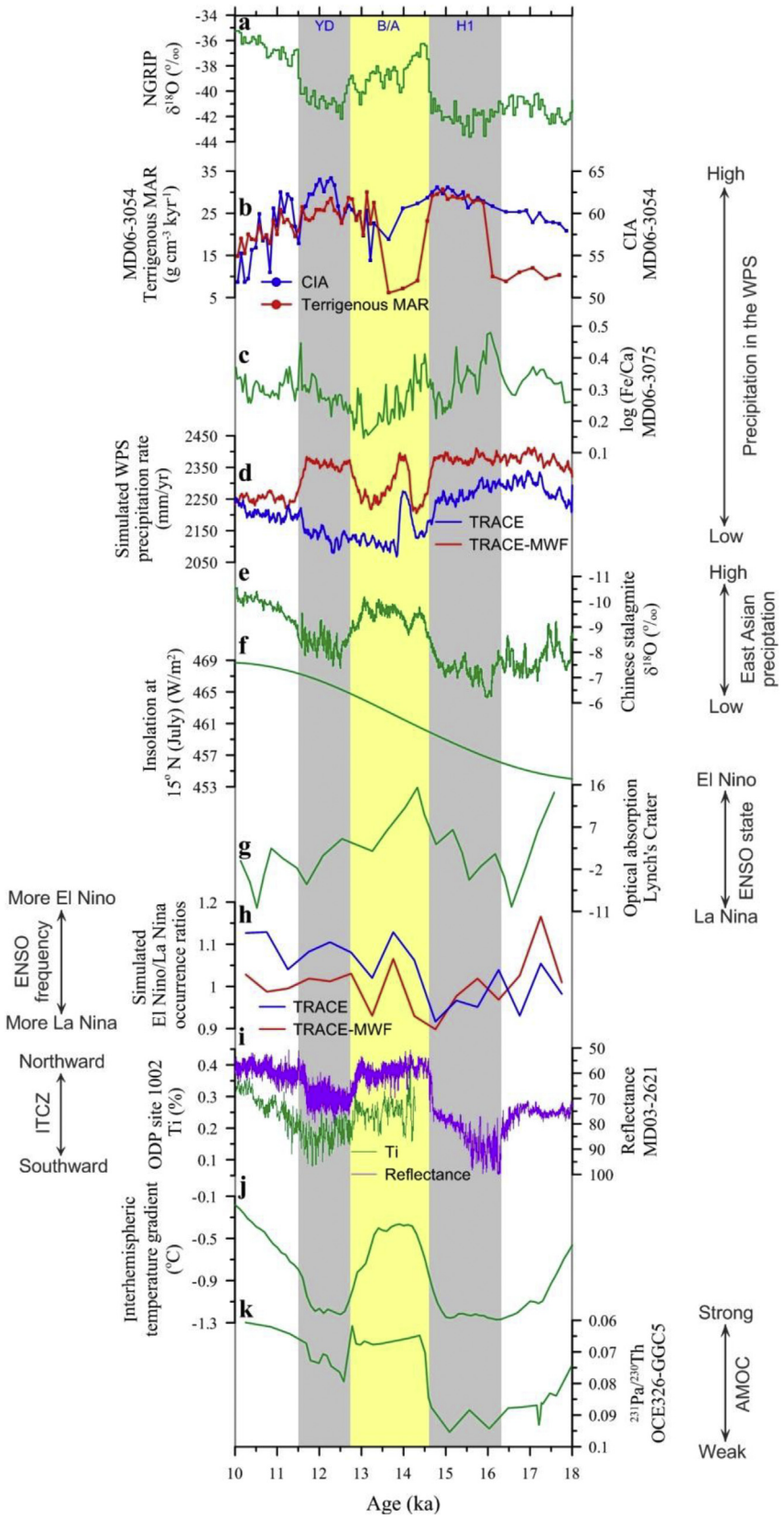

Fig. 7. (a) NGRIP $\delta^{18}O$ (Andersen et al., 2004), (b) CIA and terrigenous MAR of MD06-3054, (c) XRF core scanning record of log(Fe/Ca) in core MD06-3075 (Fraser et al., 2014), (d) simulated mean precipitation rate in the WPS by TRACE and TRACE-MWF, (e) Chinese stalagmite $\delta^{18}O$ (Wang et al., 2001, 2008), (f) local summer insolation (15 °N, July) (Laskar et al., 2004), (g) optical absorption (three point detrended) of peat sediment from Lynch's Crater (Turney et al., 2004), (h) simulated El Niño/La Niña occurrence ratios per 500 years by TRACE and TRACE-MWF, (i) Ti concentration in ODP site 1002 (Haug et al., 2001) and reflectance of core MD03-2621 (Deplazes et al., 2013), (j) interhemispheric temperature gradient (Shakun et al., 2012), and (k) $^{231}Pa/^{230}Th$ in core OCE326-GGC5 (McManus et al., 2004) during the last deglaciation. In (b), CIA was based on the CaO/Na_2O method (McLennan, 1993), and terrigenous MAR was estimated by equation (4).

during the last deglaciation (Fraser et al., 2014). These observations support decoupling of local rainfall (as proxied by log(X/Ca), where X is a detrital element) from large-scale seawater salinity changes due to evaporation, mixing and advection of ocean water masses (as reflected by $\Delta\delta^{18}O_{sw\text{-}iv}$) (Fraser et al., 2014; Gibbons et al., 2014). We infer that the terrestrial proxy log(X/Ca) is a more straightforward and robust indicator of local rainfall and erosion rates than the marine proxy $\Delta\delta^{18}O_{sw\text{-}iv}$.

Precipitation is subject to multiple forcings, including orbital (i.e., solar insolation), North Atlantic (i.e., AMOC), greenhouse gas, ENSO, and volcanic influences at a range of timescales (Mohtadi et al., 2016). At millennial timescales (e.g., during the last deglaciation), control of WPS rainfall by solar insolation is improbable. Local summer solar insolation (15°N, July) increased only gradually by ~15 W/m^2 during this interval (Fig. 7f). The ENSO certainly operated in the tropical Pacific during the last deglaciation (Tudhope et al., 2001; Koutavas et al., 2002), but there is controversy regarding whether the El Niño or La Niña state dominated during the H1 and YD. Evidence from planktonic foraminiferal Mg/Ca and $\delta^{18}O$ in the tropical West Pacific supports a persistent El Niño state during the H1 and/or YD (Stott et al., 2002; Bolliet et al., 2011). In contrast, surface moisture records based on the degree of peat humification from northern Australia suggest a dominant La Niña state during the H1 and YD (Fig. 7g) (Turney et al., 2004). The latter is more consistent with local rainfall records for the WPS, which implies the existence of a persistent La Niña state in the tropical West Pacific during the H1 and YD.

Higher rainfall in the WPS is consistent with the cessation of the AMOC during H1 and a major decline during the YD (McManus et al., 2004) (Fig. 7k), suggesting that changes of AMOC strength during the last deglaciation had global climatic impacts. The slowdown or shutdown of AMOC during the H1 and YD reduced northward heat transport within the North Atlantic, which was compensated by increased northward heat transport through the atmosphere via southward displacement of the ITCZ (Fig. 7i) (Gibbons et al., 2014; McGee et al., 2014). Reduced heat transport by the AMOC also caused a reduction in the interhemispheric SST gradient (Fig. 7j) (Shakun et al., 2012). This may have been a key factor in triggering rapid precipitation changes in the WPS during the last deglaciation. However, standard ITCZ theory calls for reduced rainfall over the northern tropics as a result of southward displacement of the ITCZ, which cannot explain rapid precipitation changes in the WPS (Broccoli et al., 2006; Schneider et al., 2014). Therefore, we invoke the ENSO as a mechanism to link AMOC changes to precipitation variability in the WPS during the last deglaciation. Indeed, model results suggest that weakening of the AMOC can reduce ENSO variability (Timmermann et al., 2005; Atwood, 2015), which is consistent with evidence of a persistent La Niña state in the tropical West Pacific during the H1 and YD (Fig. 7g, k) (Turney et al., 2004). In addition, both TRACE and TRACE-MWF yield simulated El Niño/La Niña occurrence ratios that are lower during the H1 and YD than the B/A, supporting the inference of more frequent La Niña events during the H1 and YD (Fig. 7h). We infer that the La Niña state was accompanied by intensified Walker circulation, strong easterly trade winds, and a shift in the center of tropical convection toward the West Pacific, resulting in the westward displacement of the rainfall belt over Indonesia, the Philippines, and Australia (Ropelewski and Halpert, 1987; Trenberth, 2013). This scenario can also explain the observation of reversed phases of precipitation between eastern China and the WPS during the last deglaciation (Fig. 7b, c and e). The ENSO can alter anticyclone activity in the northwestern Pacific and consequently influence the intensity of the East Asian summer monsoon (EASM) (Wu et al., 2003; Shi et al., 2012). During the H1 and YD, a reduced EASM under the La Niña state resulted in southward migration of the ITCZ over East Asia, thus increasing precipitation in southern East Asia including the WPS (Fig. 7b and c), and reducing precipitation in northern East Asia including eastern China (Fig. 7e) (Wu et al., 2003; Shi et al., 2012). Uncovering details behind this forcing mechanism will require more high-resolution tropical climate records.

To assess the robustness of our hypothesis regarding North Atlantic forcings in the WPS and tropical West Pacific during the last deglaciation, we undertook a comparison of model results with various proxy records. We compiled rainfall records from the tropical West Pacific for this interval, including records derived from stalagmite $\delta^{18}O$ and terrestrial proxies rather than $\Delta\delta^{18}O_{sw\text{-}iv}$, because the latter proxy is subject to other influences in addition to rainfall (see above). Based on TRACE and TRACE-MWF simulations for the last deglaciation, mean annual precipitation (MAP) in the WPS is shown in Fig. 7d, and MAP anomalies for the tropical West Pacific in Fig. 8. The TRACE-MWF results are more consistent with the rainfall proxy records than the TRACE results. For example, TRACE-MWF shows a positive MAP anomaly (Fig. 8c and d) whereas TRACE shows a negative MAP anomaly (Fig. 8a and b) in the WPS during the H1 and YD. The former pattern is consistent with proxy reconstructions of precipitation from Fraser et al. (2014) and the present study (Fig. 7b and c). Another climate proxy that agrees more closely with TRACE-MWF than TRACE is the Chinese stalagmite $\delta^{18}O$ record (Wang et al., 2001, 2008), which indicates dry conditions in northern East Asia during the H1 and YD (Fig. 7e).

The data-model comparisons described above are consistent with AMOC forcing of climate change in tropical West Pacific during the last deglaciation. During the last deglaciation, the sharp precipitation peak at ~14 ka in both TRACE and TRACE-MWF (Fig. 7d) may have been induced by a (simulated) AMOC overshoot resulting from a sudden termination of freshwater discharge into the North Atlantic before the BA (Liu et al., 2009a; He, 2011). Apart from this, TRACE-MWF shows rapid rainfall changes with high values during the H1 and YD, and low values during the B/A (Fig. 7d). However, TRACE does not show typical rapid rainfall changes during the last deglaciation (Fig. 7d). The excellent correspondence of rainfall records to TRACE-MWF results (Fig. 8c and d) suggests that rapid precipitation changes in the tropical West Pacific during the last deglaciation were dominantly driven by AMOC rather than other climatic factors.

The TRACE-MWF results provide further insights concerning the processes (ENSO and ITCZ) by which AMOC changes controlled rapid precipitation changes in the tropical West Pacific during the last deglaciation. Enhanced rainfall in southern Indonesia and northern Australia during the H1 (or HS1, i.e., Heinrich stadial 1) and/or YD (Muller et al., 2008, 2012; Griffiths et al., 2009; Shiau et al., 2011; Ayliffe et al., 2013; Denniston et al., 2013) is consistent with model results showing a southward shift of the ITCZ (Fig. 8). The same applies for dry conditions reported from northern Indonesia during the H1 (or HS1) and/or YD (Partin et al., 2007; Carolin et al., 2013). However, the model simulations and proxy records obtained from our study core as well as from core MD06-3075 on the Mindanao Shelf (Fraser et al., 2014) indicate that the tropical West Pacific between 6 and 22 °N (including the WPS) experienced heavy rainfall during the H1 and YD (Fig. 8), which is inconsistent with a southward shift of the ITCZ but consistent with a persistent La Niña state. Overall, both model results and proxy records indicate that precipitation changes in the tropical West Pacific cannot be explained by expansion or contraction of the ITCZ during the last deglaciation (Fig. 8). These observations suggest that rapid hydrological changes in the tropical West Pacific during the last deglaciation were ultimately controlled by North Atlantic forcings, and that the climate response was more complex than a simple meridional shift or expansion/contraction of the ITCZ and

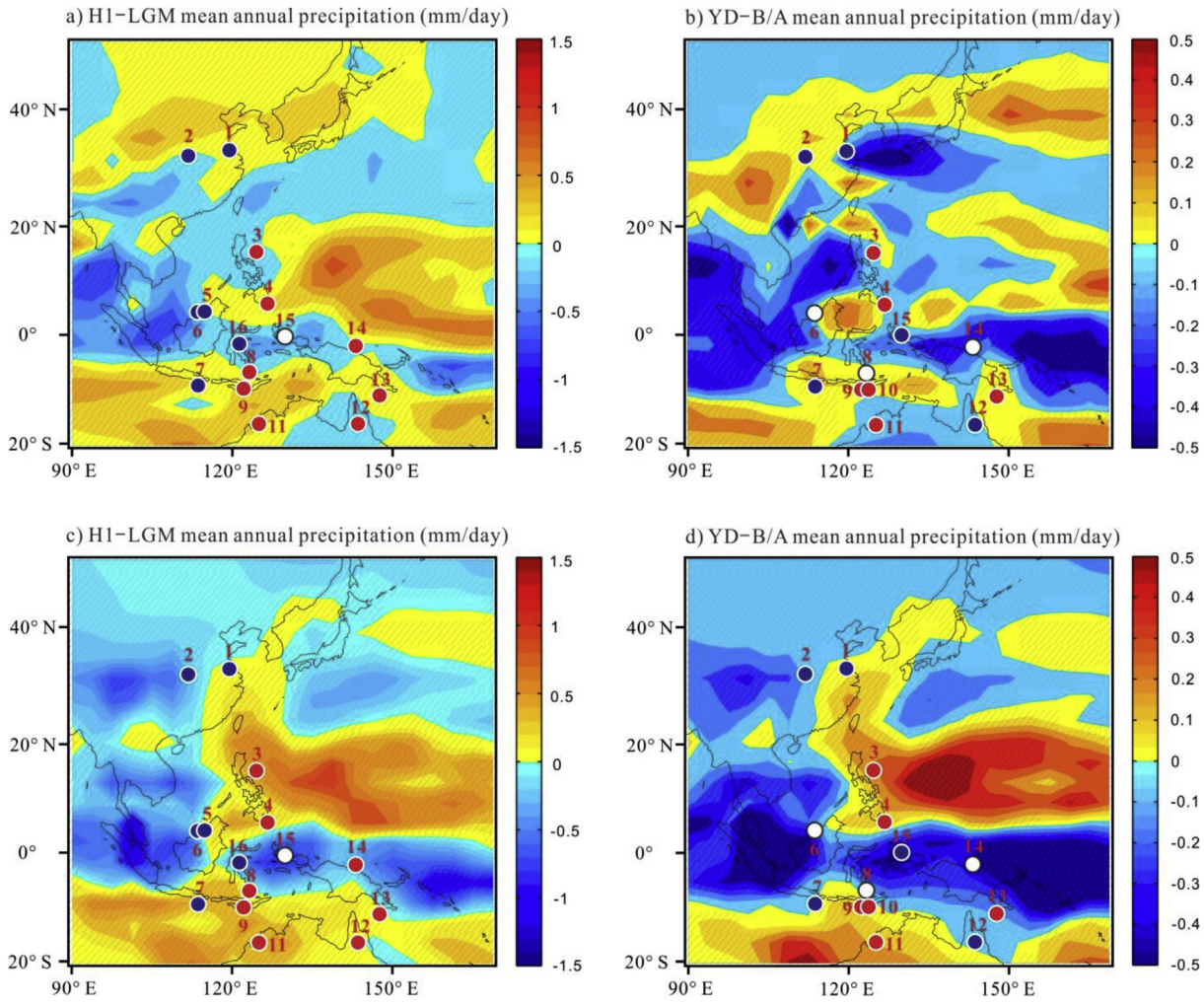

Fig. 8. TRACE (a, b) and TRACE-MWF (c, d) simulation results of mean annual precipitation anomaly in tropical West Pacific during the H1 (a, c) and YD (b, d). The hashed zones are significant at the 95% level. In order to compare, the proxy results of precipitation in tropical West Pacific were projected on the simulation map. Red and blue dots indicate increased and decreased rainfall during the H1 and YD, respectively. White dots indicate no change or uncertain changes on the rainfall during H1 and YD. Data sources for rainfall proxy records: 1. Hulu cave (Wang et al., 2001), 2. Sanbao cave (Wang et al., 2008), 3. Core MD06-3054 (this study), 4. Core MD06-3075 (Fraser et al., 2014), 5. Gunung Buda cave (Carolin et al., 2013), 6. Gunung Buda cave (Partin et al., 2007), 7. Core GeoB 10053−7 (Mohtadi et al., 2011), 8. Core VM33-80 (Muller et al., 2012), 9. Liang Luar cave (Ayliffe et al., 2013), 10. Liang Luar cave (Griffiths et al., 2009), 11. Ball Gown cave (Denniston et al., 2013), 12. Lynch's Crater (Muller et al., 2008), 13. Core MD05-2928 (Shiau et al., 2011), 14. Core MD05-2920 (Tachikawa et al., 2011), 15. Core MD10-3340 (Dang et al., 2015), and 16. Lake Towuti (Russell et al., 2014). (For interpretation of the references to colour in this figure legend, the reader is referred to the Web version of this article.)

probably included zonal shifts in precipitation linked to the ENSO and Walker circulation.

6. Conclusions

Based on a comprehensive study of secular variations of geochemical proxies in core MD06-3054 combined with model simulations, we identified rapid hydroclimatic changes in the western Philippine Sea (WPS) region during the last deglaciation and evaluated their forcing mechanisms. Detrital siliciclastics in marine sediments on the outer western Luzon Shelf were derived mainly from weathering of volcanic rocks of Luzon. The degree of chemical weathering of sediments deposited during the LGM and the Holocene was apparently similar, mainly due to reworking of inner-shelf sediments exposed during the LGM eustatic lowstand. Terrigenous inputs were declined from the LGM to the Holocene as a result of gradually rising sea level. Rapid variations in chemical weathering intensity and terrigenous fluxes during the last deglaciation were not linked to sea-level or temperature changes but, rather, to local rainfall changes on Luzon. Rapid fluctuations in precipitation during the last deglaciation are supported by terrestrial proxy records from the Mindanao Shelf but in conflict with $\Delta\delta^{18}O_{sw\text{-}iv}$ records from the WPS. However, $\Delta\delta^{18}O_{sw\text{-}iv}$ may be controlled mainly by changes in the regional hydrologic cycle rather than local rainfall. High rainfall in the WPS during the H1 and YD was not due to the southward shift of the ITCZ at those times, but, rather, it was probably linked to the development of a persistent La Niña state in the tropical Pacific in response to reduced AMOC. Variations in precipitation during the last deglaciation at sites across the tropical West Pacific can be linked to AMOC strength, an interpretation that is consistent with climate modeling results. The influence of AMOC strength on the tropical West Pacific was probably propagated through meridional and zonal shifts in precipitation linked to the ITCZ and ENSO, respectively.

Data availability

Datasets related to this article can be found at https://doi.org/10.

17632/t2y8s77ghp.1, an open-source online data repository hosted at Mendeley Data (Xiong et al., 2018).

Acknowledgments

We thank the chief scientist, Carlo Laj, the captain and crew of *R/V* Marion Dufresne, and the French Polar Institute for their effort and support during the IMAGES XIV-MD155-Marco Polo 2 cruise. We are grateful to Mahyar Mohtadi for helpful discussions on monsoon rainfall, and to Zhengyu Liu for assistance with model simulations. This study was supported by the Open Fund of Qingdao National Laboratory for Marine Science and Technology (grant no. QNLM2016ORP0205), Basic Scientific Fund for National Public Research Institutes of China (grant no. 2017Y07), National Natural Science Foundation of China (grant nos. 41230959, 41106042, 41576051, and 41476041), Scientific and Technological Innovation Project of Qingdao National Laboratory for Marine Science and Technology (grant no. 2016ASKJ13), and National Special Project for Global Change and Air-Sea Interaction (grant no. GASI-GEOGE-04). PDC thanks the Charles T. McCord Chair in Petroleum Geology for support during development of this study.

Appendix A. Supplementary data

Supplementary data related to this article can be found at https://doi.org/10.1016/j.quascirev.2018.07.040.

References

Andersen, K.K., Azuma, N., Barnola, J.M., Bigler, M., Biscaye, P., Caillon, N., Chappellaz, J., Clausen, H.B., Dahl-Jensen, D., Fischer, H., Fluckiger, J., Fritzsche, D., Fujii, Y., Goto-Azuma, K., Gronvold, K., Gundestrup, N.S., Hansson, M., Huber, C., Hvidberg, C.S., Johnsen, S.J., Jonsell, U., Jouzel, J., Kipfstuhl, S., Landais, A., Leuenberger, M., Lorrain, R., Masson-Delmotte, V., Miller, H., Motoyama, H., Narita, H., Popp, T., Rasmussen, S.O., Raynaud, D., Rothlisberger, R., Ruth, U., Samyn, D., Schwander, J., Shoji, H., Siggard-Andersen, M.L., Steffensen, J.P., Stocker, T., Sveinbjornsdottir, A.E., Svensson, A., Takata, M., Tison, J.L., Thorsteinsson, T., Watanabe, O., Wilhelms, F., White, J.W., 2004. High-resolution record of Northern Hemisphere climate extending into the last interglacial period. Nature 431, 147–151.

Arz, H.W., Pätzold, J., Wefer, G., 1999. Climatic changes during the last deglaciation recorded in sediment cores from the northeastern Brazilian Continental Margin. Geo Mar. Lett. 19, 209–218.

Atwood, A.R., 2015. Mechanisms of Tropical Pacific Climate Change during the Holocene. Ph.D. dissertation. University of Washington, p. 198.

Ayliffe, L.K., Gagan, M.K., Zhao, J.-x., Drysdale, R.N., Hellstrom, J.C., Hantoro, W.S., Griffiths, M.L., Scott-Gagan, H., Pierre, E.S., Cowley, J.A., Suwargadi, B.W., 2013. Rapid interhemispheric climate links via the Australasian monsoon during the last deglaciation. Nat. Commun. 4, 2908. https://doi.org/10.1038/ncomms3908.

Bard, E., Hamelin, B., Arnold, M., Montaggioni, L., Cabioch, G., Faure, G., Rougerie, F., 1996. Deglacial sea-level record from Tahiti corals and the timing of global meltwater discharge. Nature 382, 241–244.

Bard, E., Hamelin, B., Delanghe-Sabatier, D., 2010. Deglacial meltwater pulse 1B and Younger Dryas sea levels revisited with boreholes at Tahiti. Science 327, 1235–1237.

Bayon, G., Barrat, J.A., Etoubleau, J., Benoit, M., Bollinger, C., Révillon, S., 2009. Determination of rare earth elements, Sc, Y, Zr, Ba, Hf and Th in geological samples by ICP-MS after Tm addition and alkaline fusion. Geostand. Geoanal. Res. 33, 51–62.

Bellwood, P., Dizon, E., 2013. 4000 Years of Migration and Cultural Exchange: the Archaeology of the Batanes Islands, Northern Philippines. Australian National University Press, Canberra, p. 254.

Berger, W.H., Bonneau, M.C., Parker, F.L., 1982. Foraminifera on the deep-sea floor-lysocline and dissolution rate. Oceanol. Acta 5, 249–258.

Bolliet, T., Holbourn, A., Kuhnt, W., Laj, C., Kissel, C., Beaufort, L., Kienast, M., Andersen, N., Garbe-Schönberg, D., 2011. Mindanao dome variability over the last 160 kyr: episodic glacial cooling of the west Pacific warm pool. Paleoceanography 26, PA1208. https://doi.org/10.1029/2010PA001966.

Boulay, S., Colin, C., Trentesaux, A., Clain, S., Liu, Z., Lauer-Leredde, C., 2007. Sedimentary responses to the Pleistocene climatic variations recorded in the South China Sea. Quat. Res. 68, 162–172.

Broccoli, A.J., Dahl, K.A., Stouffer, R.J., 2006. Response of the ITCZ to northern Hemisphere cooling. Geophys. Res. Lett. 33, L01702. https://doi.org/10.1029/2005GL024546.

Byrne, M.P., Schneider, T., 2016. Energetic constraints on the width of the inter-tropical convergence zone. J. Clim. 29, 4709–4721.

Carolin, S.A., Cobb, K.M., Adkins, J.F., Clark, B., Conroy, J.L., Lejau, S., Malang, J., Tuen, A.A., 2013. Varied response of western Pacific hydrology to climate forcings over the last glacial period. Science 340, 1564–1566.

Chang, F., Li, T., Xiong, Z., Xu, Z., 2015. Evidence for sea level and monsoonally driven variations in terrigenous input to the northern East China Sea during the last 24.3 ka. Paleoceanography 30, 642–658.

Chen, S., Li, T., Tang, Z., Qiu, X., Xiong, Z., Nan, Q., Xu, Z., Chang, F., 2011. Response of the northwestern Pacific upper water $\delta^{13}C$ to the last deglacial ventilation of the deep southern ocean. Chin. Sci. Bull. 56, 2628–2634.

Chiang, J.C.H., 2009. The tropics in paleoclimate. Annu. Rev. Earth Planet Sci. 37, 263–297.

Chiang, J.C.H., Friedman, A.R., 2012. Extratropical cooling, interhemispheric thermal gradients, and tropical climate change. Annu. Rev. Earth Planet Sci. 40, 383–412.

Clark, P.U., McCabe, A.M., Mix, A.C., Weaver, A.J., 2004. Rapid rise of sea level 19,000 years ago and its global implications. Science 304, 1141–1144.

Clift, P.D., 2006. Controls on the erosion of Cenozoic Asia and the flux of clastic sediment to the ocean. Earth Planet Sci. Lett. 241, 571–590.

Clift, P.D., Wan, S., Blusztajn, J., 2014. Reconstructing chemical weathering, physical erosion and monsoon intensity since 25 Ma in the northern South China Sea: a review of competing proxies. Earth Sci. Rev. 130, 86–102.

Dang, H., Jian, Z., Bassinot, F., 2009. Turbidite deposition of the last glacial stage in the western Philippine Sea and its paleoenviromental implications. Quat. Sci. 29, 1078–1085 (in Chinese with English abstract).

Dang, H., Jian, Z., Kissel, C., Bassinot, F., 2015. Precessional changes in the western equatorial Pacific hydroclimate: a 240 kyr marine record from the Halmahera Sea, East Indonesia. G-cubed 16, 148–164.

Defant, M.J., Maury, R., Joron, J.-L., Feigenson, M.D., Leterrier, J., Bellon, H., Jacques, D., Richard, M., 1990. The geochemistry and tectonic setting of the northern section of the Luzon arc (The Philippines and Taiwan). Tectonophysics 183, 187–205.

Denniston, R.F., Ummenhofer, C.C., Wanamaker, A.D., Lachniet, M.S., Villarini, G., Asmerom, Y., Polyak, V.J., Passaro, K.J., Cugley, J., Woods, D., Humphreys, W.F., 2016. Expansion and contraction of the Indo-Pacific tropical rain belt over the last three millennia. Sci. Rep. 6, 34485. https://doi.org/10.1038/srep34485.

Denniston, R.F., Wyrwoll, K.-H., Asmerom, Y., Polyak, V.J., Humphreys, W.F., Cugley, J., Woods, D., LaPointe, Z., Peota, J., Greaves, E., 2013. North Atlantic forcing of millennial-scale Indo-Australian monsoon dynamics during the Last Glacial period. Quat. Sci. Rev. 72, 159–168.

Deplazes, G., Luckge, A., Peterson, L.C., Timmermann, A., Hamann, Y., Hughen, K.A., Rohl, U., Laj, C., Cane, M.A., Sigman, D.M., Haug, G.H., 2013. Links between tropical rainfall and North Atlantic climate during the last glacial period. Nat. Geosci. 6, 213–217.

Deschamps, P., Durand, N., Bard, E., Hamelin, B., Camoin, G., Thomas, A.L., Henderson, G.M., Okuno, J.I., Yokoyama, Y., 2012. Ice-sheet collapse and sea-level rise at the Bolling warming 14,600 years ago. Nature 483, 559–564.

Dou, Y., Yang, S., Shi, X., Clift, P.D., Liu, S., Liu, J., Li, C., Bi, L., Zhao, Y., 2016. Provenance weathering and erosion records in southern Okinawa Trough sediments since 28 ka: geochemical and Sr-Nd-Pb isotopic evidences. Chem. Geol. 425, 93–109.

Fedo, C.M., Nesbitt, H.W., Young, G.M., 1995. Unraveling the effects of potassium metasomatism in sedimentary rocks and paleosols, with implications for paleoweathering conditions and provenance. Geology 23, 921–924.

Fine, R.A., Lukas, R., Bingham, F.M., Warner, M.J., Gammon, R.H., 1994. The western equatorial Pacific: a water mass crossroads. J. Geophys. Res. 99, 25063–25080.

Fraser, N., Kuhnt, W., Holbourn, A., Bolliet, T., Andersen, N., Blanz, T., Beaufort, L., 2014. Precipitation variability within the west Pacific warm pool over the past 120 ka: evidence from the Davao Gulf, southern Philippines. Paleoceanography 29, 1094–1110.

Gibbons, F.T., Oppo, D.W., Mohtadi, M., Rosenthal, Y., Cheng, J., Liu, Z., Linsley, B.K., 2014. Deglacial $\delta^{18}O$ and hydrologic variability in the tropical Pacific and indian oceans. Earth Planet Sci. Lett. 387, 240–251.

Gislason, S.R., Oelkers, E.H., Eiriksdottir, E.S., Kardjilov, M.I., Gisladottir, G., Sigfusson, B., Snorrason, A., Elefsen, S., Hardardottir, J., Torssander, P., Oskarsson, N., 2009. Direct evidence of the feedback between climate and weathering. Earth Planet Sci. Lett. 277, 213–222.

Govin, A., Chiessi, C.M., Zabel, M., Sawakuchi, A.O., Heslop, D., Hoerner, T., Zhang, Y., Mulitza, S., 2014. Terrigenous input off northern South America driven by changes in Amazonian climate and the North Brazil Current retroflection during the last 250 ka. Clim. Past 10, 843–862.

Griffiths, M.L., Drysdale, R.N., Gagan, M.K., Zhao, J.X., Ayliffe, L.K., Hellstrom, J.C., Hantoro, W.S., Frisia, S., Feng, Y.X., Cartwright, I., Pierre, E.S., Fischer, M.J., Suwargadi, B.W., 2009. Increasing Australian-Indonesian monsoon rainfall linked to early Holocene sea-level rise. Nat. Geosci. 2, 636–639.

Griffiths, M.L., Drysdale, R.N., Vonhof, H.B., Gagan, M.K., Zhao, J., Ayliffe, L.K., Hantoro, W.S., Hellstrom, J.C., Cartwright, I., Frisia, S., Suwargadi, B.W., 2010. Younger Dryas–Holocene temperature and rainfall history of southern Indonesia from $\delta^{18}O$ in speleothem calcite and fluid inclusions. Earth Planet Sci. Lett. 295, 30–36.

Groetsch, J., Wu, G., Berger, W.H., 1991. Carbonate saturation cycles in the western equatorial Pacific. In: Einsele, G., Ricken, W., Seilacher, A. (Eds.), Cycles and Events in Stratigraphy. Springer, Heidelberg, pp. 110–125.

Hanebuth, T., Stattegger, K., Grootes, P.M., 2000. Rapid flooding of the Sunda Shelf: a late-glacial sea-level record. Science 288, 1033–1035.

Haug, G.H., Hughen, K.A., Sigman, D.M., Peterson, L.C., Rohl, U., 2001. Southward

migration of the intertropical convergence zone through the Holocene. Science 293, 1304–1308.
He, F., 2011. Simulating Transient Climate Evolution of the Last Deglaciation with CCSM3. Ph.D. dissertation. University of Wisconsin-Madison, p. 171.
Hu, D., Clift, P.D., Böning, P., Hannigan, R., Hillier, S., Blusztajn, J., Wan, S., Fuller, D.Q., 2013. Holocene evolution in weathering and erosion patterns in the Pearl River delta. G-cubed 14, 2349–2368.
Hu, D., Clift, P.D., Wan, S., Böning, P., Hannigan, R., Hillier, S., Blusztajn, J., 2016. Testing chemical weathering proxies in miocene-recent fluvial-derived sediments in the South China sea. In: Clift, P.D., Harff, J., Wu, J., Qui, Y. (Eds.), River-dominated Shelf Sediments of East Asian Seas, vol. 429. Geological Society of London, Special Publication, pp. 45–72.
Hu, Z., Gao, S., 2008. Upper crustal abundances of trace elements: a revision and update. Chem. Geol. 253, 205–221.
Jacobsen, S.B., Wasserburg, G.J., 1980. Sm-Nd isotopic evolution of chondrites. Earth Planet Sci. Lett. 50, 139–155.
Jahn, B.-M., Gallet, S., Han, J., 2001. Geochemistry of the Xining, Xifeng and Jixian sections, Loess Plateau of China: eolian dust provenance and paleosol evolution during the last 140 ka. Chem. Geol. 178, 71–94.
Jia, G., Bai, Y., Yang, X., Xie, L., Wei, G., Ouyang, T., Chu, G., Liu, Z., Peng, P., 2015. Biogeochemical evidence of Holocene East Asian summer and winter monsoon variability from a tropical maar lake in southern China. Quat. Sci. Rev. 111, 51–61.
Jiang, F., Frank, M., Li, T., Chen, T.-Y., Xu, Z., Li, A., 2013. Asian dust input in the western Philippine Sea: evidence from radiogenic Sr and Nd isotopes. G-cubed 14, 1538–1551.
Jiang, F., Zhou, Y., Nan, Q., Zhou, Y., Zheng, X., Li, T., Li, A., Wang, H., 2016. Contribution of Asian dust and volcanic material to the western Philippine Sea over the last 220 kyr as inferred from grain size and Sr-Nd isotopes. J. Geophys. Res. 121 https://doi.org/10.1002/2016JC012000.
Kissel, C., Laj, C., Kienast, M., Bolliet, T., Holbourn, A., Hill, P., Kuhnt, W., Braconnot, P., 2010. Monsoon variability and deep oceanic circulation in the western equatorial Pacific over the last climatic cycle: insights from sedimentary magnetic properties and sortable silt. Paleoceanography 25, PA3215. https://doi.org/10.1029/2010PA001980.
Koutavas, A., Lynch-Stieglitz, J., Marchitto, T.M., Sachs, J.P., 2002. El Niño-like pattern in ice age tropical Pacific sea surface temperature. Science 297, 226–230.
Kump, L.R., Brantley, S.L., Arthur, M.A., 2000. Chemical weathering, atmospheric CO_2, and climate. Annu. Rev. Earth Planet Sci. 28, 611–667.
Laj, C., Shipboard Scientific Party, 2006. MD155-Marco Polo 2, IMAGES XIV Cruise Report. Publications de l'Institut Polaire Francais. OCE/2006/06.
Laskar, J., Robutel, P., Joutel, F., Gastineau, M., Correia, A., Levrard, B., 2004. A long-term numerical solution for the insolation quantities of the Earth. Astron. Astrophys. 428, 261–285.
Latimer, J.C., Filippelli, G.M., 2001. Terrigenous input and paleoproductivity in the southern ocean. Paleoceanography 16, 627–643.
Leduc, G., Vidal, L., Tachikawa, K., Bard, E., 2009. ITCZ rather than ENSO signature for abrupt climate changes across the tropical Pacific? Quat. Res. 72, 123–131.
Levi, C., Labeyrie, L., Bassinot, F., Guichard, F., Cortijo, E., Waelbroeck, C., Caillon, N., Duprat, J., de Garidel-Thoron, T., Elderfield, H., 2007. Low-latitude hydrological cycle and rapid climate changes during the last deglaciation. G-cubed 8, Q05N12. https://doi.org/10.1029/2006GC001514.
Limmer, D.R., Boening, P., Giosan, L., Ponton, C., Koehler, C.M., Cooper, M.J., Tabrez, A.R., Clift, P.D., 2012. Geochemical record of Holocene to recent sedimentation on the western Indus continental shelf, Arabian Sea. G-cubed 13, Q01008. https://doi.org/10.1029/2011GC003845.
Liu, J.P., Milliman, J.D., Gao, S., Cheng, P., 2004. Holocene development of the yellow river's subaqueous delta, north yellow sea. Mar. Geol. 209, 45–67.
Liu, Z., Otto-Bliesner, B.L., He, F., Brady, E.C., Tomas, R., Clark, P.U., Erickson, D., 2009a. Transient simulation of last deglaciation with a new mechanism for Bølling-Allerød warming. Science 325, 310–314.
Liu, Z., Zhao, Y., Colin, C., Siringan, F.P., Wu, Q., 2009b. Chemical weathering in Luzon, Philippines from clay mineralogy and major-element geochemistry of river sediments. Appl. Geochem. 24, 2195–2205.
Liu, Z., Lu, Z., Wen, X., Otto-Bliesner, B.L., Timmermann, A., Cobb, K.M., 2014. Evolution and forcing mechanisms of El Nino over the past 21,000 years. Nature 515, 550–553.
Liu, Z., Zhao, Y., Colin, C., Stattegger, K., Wiesner, M.G., Huh, C.-A., Zhang, Y., Li, X., Sompongchaiyakul, P., You, C.-F., Huang, C.-Y., Liu, J.T., Siringan, F.P., Le, K.P., Sathiamurthy, E., Hantoro, W.S., Liu, J., Tuo, S., Zhao, S., Zhou, S., He, Z., Wang, Y., Bunsomboonsakul, S., Li, Y., 2016. Source-to-sink transport processes of fluvial sediments in the South China Sea. Earth Sci. Rev. 153, 238–273.
Lupker, M., France-Lanord, C., Galy, V., Lavé, J., Kudrass, H., 2013. Increasing chemical weathering in the Himalayan system since the Last Glacial Maximum. Earth Planet Sci. Lett. 365, 243–252.
Lyon, B., Cristi, H., Verceles, E.R., Hilario, F.D., Abastillas, R., 2006. Seasonal reversal of the ENSO rainfall signal in the Philippines. Geophys. Res. Lett. 33, L24710. https://doi.org/10.1029/2006GL028182.
Martinez, N.C., Murray, R.W., Thunell, R.C., Peterson, L.C., Muller-Karger, F., Astor, Y., Varela, R., 2007. Modern climate forcing of terrigenous deposition in the tropics (Cariaco Basin, Venezuela). Earth Planet Sci. Lett. 264, 438–451.
McGee, D., Donohoe, A., Marshall, J., Ferreira, D., 2014. Changes in ITCZ location and cross-equatorial heat transport at the Last Glacial Maximum, Heinrich stadial 1, and the mid-Holocene. Earth Planet Sci. Lett. 390, 69–79.
McLennan, S.M., 1993. Weathering and global denudation. J. Geol. 101, 295–303.
McManus, J.F., Francois, R., Gherardi, J.M., Keigwin, L.D., Brown-Leger, S., 2004. Collapse and rapid resumption of Atlantic meridional circulation linked to deglacial climate changes. Nature 428, 834–837.
Merkel, U., Prange, M., Schulz, M., 2010. ENSO variability and teleconnections during glacial climates. Quat. Sci. Rev. 29, 86–100.
Mijares, A.S., Détroit, F., Piper, P., Grün, R., Bellwood, P., Aubert, M., Champion, G., Cuevas, N., De Leon, A., Dizon, E., 2010. New evidence for a 67, 000-year-old human presence at Callao cave, Luzon, Philippines. J. Hum. Evol. 59, 123–132.
Mohtadi, M., Oppo, D.W., Steinke, S., Stuut, J.-B.W., De Pol-Holz, R., Hebbeln, D., Luckge, A., 2011. Glacial to Holocene swings of the Australian-Indonesian monsoon. Nat. Geosci. 4, 540–544.
Mohtadi, M., Prange, M., Steinke, S., 2016. Palaeoclimatic insights into forcing and response of monsoon rainfall. Nature 533, 191–199.
Mollier-Vogel, E., Leduc, G., Böschen, T., Martinez, P., Schneider, R.R., 2013. Rainfall response to orbital and millennial forcing in northern Peru over the last 18 ka. Quat. Sci. Rev. 76, 29–38.
Muller, J., Kylander, M., Wüst, R.A.J., Weiss, D., Martinez-Cortizas, A., LeGrande, A.N., Jennerjahn, T., Behling, H., Anderson, W.T., Jacobson, G., 2008. Possible evidence for wet Heinrich phases in tropical NE Australia: the Lynch's Crater deposit. Quat. Sci. Rev. 27, 468–475.
Muller, J., McManus, J.F., Oppo, D.W., Francois, R., 2012. Strengthening of the northeast monsoon over the Flores sea, Indonesia, at the time of Heinrich event 1. Geology 40, 635–638.
Nesbitt, H.W., Markovics, G., 1997. Weathering of granodioritic crust, long-term storage of elements in weathering profiles, and petrogenesis of siliciclastic sediments. Geochem. Cosmochim. Acta 61, 1653–1670.
Nesbitt, H.W., Markovics, G., Price, R.C., 1980. Chemical processes affecting alkalis and alkaline earths during continental weathering. Geochem. Cosmochim. Acta 44, 1659–1666.
Nesbitt, H.W., Young, G., 1982. Early Proterozoic climates and plate motions inferred from major element chemistry of lutites. Nature 299, 715–717.
Partin, J.W., Cobb, K.M., Adkins, J.F., Clark, B., Fernandez, D.P., 2007. Millennial-scale trends in west Pacific warm pool hydrology since the Last Glacial Maximum. Nature 449, 452–455.
Peltier, W.R., Fairbanks, R.G., 2006. Global glacial ice volume and Last Glacial Maximum duration from an extended Barbados sea level record. Quat. Sci. Rev. 25, 3322–3337.
Price, J.R., Velbel, M.A., 2003. Chemical weathering indices applied to weathering profiles developed on heterogeneous felsic metamorphic parent rocks. Chem. Geol. 202, 397–416.
Qiao, Y., Hao, Q., Peng, S., Wang, Y., Li, J., Liu, Z., 2011. Geochemical characteristics of the eolian deposits in southern China, and their implications for provenance and weathering intensity. Palaeogeogr. Palaeoclimatol. Palaeoecol. 308, 513–523.
Qiu, B., 2001. Kuroshio and oyashio currents. In: Steele, J., Thorpe, S., Turekian, K. (Eds.), Encyclopedia of Ocean Sciences. Academic Press, Waltham, Massachusetts, pp. 1413–1425.
Qiu, X., Li, T., Chang, F., Nan, Q., Xiong, Z., Sun, H., 2014. Sea surface temperature and salinity reconstruction based on stable isotopes and Mg/Ca of planktonic foraminifera in the western Pacific Warm Pool during the last 155 ka. Chin. J. Oceanol. Limnol. 32, 187–200.
Ravelo, A.C., Hillaire-Marcel, C., 2007. The use of oxygen and carbon isotopes of foraminifera in paleoceanography. In: Hillaire-Marcel, C., De Vernal, A. (Eds.), Proxies in Late Cenozoic Paleoceanography, Developments in Marine Geology Series, vol. 1. Elsevier, Amsterdam, pp. 735–764.
Reimer, P.J., Bard, E., Bayliss, A., Beck, J.W., Blackwell, P.G., Ramsey, C.B., Buck, C.E., Cheng, H., Edwards, R.L., Friedrich, M., Grootes, P.M., Guilderson, T.P., Haflidason, H., Hajdas, I., Hatte, C., Heaton, T.J., Hoffmann, D.L., Hogg, A.G., Hughen, K.A., Kaiser, K.F., Kromer, B., Manning, S.W., Niu, M., Reimer, R.W., Richards, D.A., Scott, E.M., Southon, J.R., Staff, R.A., Turney, C.S.M., van der Plicht, J., 2013. IntCal13 and Marine13 radiocarbon age calibration curves 0-50000 years cal BP. Radiocarbon 55, 1869–1887.
Reitz, A., Pfeifer, K., De Lange, G., Klump, J., 2004. Biogenic barium and the detrital Ba/Al ratio: a comparison of their direct and indirect determination. Mar. Geol. 204, 289–300.
Riethdorf, J.R., Nuernberg, D., Max, L., Tiedemann, R., Gorbarenko, S.A., Malakhov, M.I., 2013. Millennial-scale variability of marine productivity and terrigenous matter supply in the western Bering Sea over the past 180 kyr. Clim. Past 9, 1345–1373.
Ropelewski, C.F., Halpert, M.S., 1987. Global and regional scale precipitation patterns associated with the El Niño/southern oscillation. Mon. Weather Rev. 115, 1606–1626.
Russell, J.M., Vogel, H., Konecky, B.L., Bijaksana, S., Huang, Y., Melles, M., Wattrus, N., Costa, K., King, J.W., 2014. Glacial forcing of central Indonesian hydroclimate since 60,000 y B.P. Proc. Natl. Acad. Sci. Unit. States Am. 111, 5100–5105.
Saikku, R., Stott, L., Thunell, R., 2009. A bi-polar signal recorded in the western tropical Pacific: northern and Southern Hemisphere climate records from the Pacific warm pool during the last Ice Age. Quat. Sci. Rev. 28, 2374–2385.
Schneider, T., Bischoff, T., Haug, G.H., 2014. Migrations and dynamics of the intertropical convergence zone. Nature 513, 45–53.
Schopka, H.H., Derry, L.A., Arcilla, C.A., 2011. Chemical weathering, river geochemistry and atmospheric carbon fluxes from volcanic and ultramafic regions on Luzon Island, the Philippines. Geochem. Cosmochim. Acta 75, 978–1002.
Schroeder, J., Murray, R., Leinen, M., Pflaum, R., Janecek, T., 1997. Barium in equatorial Pacific carbonate sediment: terrigenous, oxide, and biogenic associations.

Paleoceanography 12, 125–146.
Seo, I., Lee, Y.I., Yoo, C.M., Kim, H.J., Hyeong, K., 2014. Sr-Nd isotope composition and clay mineral assemblages in eolian dust from the central Philippine Sea over the last 600 kyr: implications for the transport mechanism of Asian dust. J. Geophys. Res. 119, 11492–11504.
Shakun, J.D., Clark, P.U., He, F., Marcott, S.A., Mix, A.C., Liu, Z., Otto-Bliesner, B., Schmittner, A., Bard, E., 2012. Global warming preceded by increasing carbon dioxide concentrations during the last deglaciation. Nature 484, 49–54.
Shao, J., Yang, S., 2012. Does chemical index of alteration (CIA) reflect silicate weathering and monsoonal climate in the Changjiang River basin? Chin. Sci. Bull. 57, 1178–1187.
Shi, Z., Liu, X., Cheng, X., 2012. Anti-phased response of northern and southern East Asian summer precipitation to ENSO modulation of orbital forcing. Quat. Sci. Rev. 40, 30–38.
Shiau, L.J., Chen, M.T., Clemens, S.C., Huh, C.A., Yamamoto, M., Yokoyama, Y., 2011. Warm pool hydrological and terrestrial variability near southern Papua New Guinea over the past 50k. Geophys. Res. Lett. 38, L00F01. https://doi.org/10.1029/2010GL045309.
Siddall, M., Rohling, E.J., Almogi-Labin, A., Hemleben, C., Meischner, D., Schmelzer, I., Smeed, D.A., 2003. Sea-level fluctuations during the last glacial cycle. Nature 423, 853–858.
Sonntag, I., Kerrich, R., Hagemann, S.G., 2011. The geochemistry of host arc volcanic rocks to the Co–O epithermal gold deposit, Eastern Mindanao, Philippines. Lithos 127, 564–580.
Steiger, R.H., Jäger, E., 1977. Subcommission on geochronology: convention on the use of decay constants in geo- and cosmochronology. Earth Planet Sci. Lett. 36, 359–362.
Steinke, S., Hanebuth, T.J.J., Vogt, C., Stattegger, K., 2008. Sea level induced variations in clay mineral composition in the southwestern South China Sea over the past 17,000 yr. Mar. Geol. 250, 199–210.
Stevenson, J., Siringan, F., Finn, J.A.N., Madulid, D., Heijnis, H., 2010. Paoay Lake, northern Luzon, the Philippines: a record of Holocene environmental change. Global Change Biol. 16, 1672–1688.
Stott, L.D., Poulsen, C., Lund, S., Thunell, R., 2002. Super ENSO and global climate oscillations at millennial time scales. Science 297, 222–226.
Stott, L.D., 2007. Comment on "Anomalous radiocarbon ages for foraminifera shells" by W. Broecker et al.: a correction to the western tropical Pacific MD9821-81 record. Paleoceanography 22, PA1211. https://doi.org/10.1029/2006PA001379.
Swift, D.J.P., Thorne, J.A., 1991. Sedimentation on Continental Margins I: a General Model for Shelf Sedimentation. Shelf Sand and Sandstone Bodies, 14, pp. 3–31.
Tachikawa, K., Cartapanis, O., Vidal, L., Beaufort, L., Barlyaeva, T., Bard, E., 2011. The precession phase of hydrological variability in the Western Pacific Warm Pool during the past 400 ka. Quat. Sci. Rev. 30, 3716–3727.
Tanaka, T., Togashi, S., Kamioka, H., Amakawa, H., Kagami, H., Hamamoto, T., Yuhara, M., Orihashi, Y., Yoneda, S., Shimizu, H., Kunimaru, T., Takahashi, K., Yanagi, T., Nakano, T., Fujimaki, H., Shinjo, R., Asahara, Y., Tanimizu, M., Dragusanu, C., 2000. JNdi-1: a neodymium isotopic reference in consistency with LaJolla neodymium. Chem. Geol. 168, 279–281.
Taylor, S.R., McLennan, S.M., McCulloch, M.T., 1983. Geochemistry of loess, continental crustal composition and crustal model ages. Geochem. Cosmochim. Acta 47, 1897–1905.
Thompson, L.G., Mosley-Thompson, E., Davis, M.E., Lin, P.-N., Henderson, K.A., Cole-Dai, J., Bolzan, J.F., Liu, K.-B., 1995. Late glacial stage and Holocene tropical ice core records from Huascaran, Peru. Science 269, 46–50.
Thompson, L.G., Davis, M.E., Mosley-Thompson, E., Sowers, T., Henderson, K.A., Zagorodnov, V.S., Lin, P.-N., Mikhalenko, V.N., Campen, R.K., Bolzan, J.F., 1998. A 25,000-year tropical climate history from Bolivian ice cores. Science 282, 1858–1864.
Timmermann, A., An, S., Krebs, U., Goosse, H., 2005. ENSO suppression due to weakening of the North Atlantic thermohaline circulation. J. Clim. 18, 3122–3139.
Trenberth, K.E., 2013. El Niño southern oscillation (ENSO). In: Elias, S. (Ed.), Reference Module in Earth Systems and Environmental Sciences. Elsevier, London, pp. 1–12.
Tudhope, A.W., Chilcott, C.P., McCulloch, M.T., Cook, E.R., Chappell, J., Ellam, R.M., Shimmield, G.B., 2001. Variability in the El Niño-southern oscillation through a glacial-interglacial cycle. Science 291, 1511–1517.
Turney, C.S.M., Kershaw, A.P., Clemens, S.C., Branch, N., Moss, P.T., Keith Fifield, L., 2004. Millennial and orbital variations of El Nino/Southern Oscillation and high-latitude climate in the last glacial period. Nature 428, 306–310.
Walia, M., Yang, T.F., Knittel, U., Liu, T.K., Lo, C.H., Chung, S.L., Teng, L.S., Dimalanta, C.B., Yumul Jr., G.P., Yuan, W.M., 2013. Cenozoic tectonics in the Buruanga Peninsula, Panay Island, Central Philippines, as constrained by U-Pb, $^{40}Ar/^{39}Ar$ and fission track thermochronometers. Tectonophysics 582, 205–220.
Wan, S., Yu, Z., Clift, P.D., Sun, H., Li, A., Li, T., 2012. History of Asian eolian input to the West Philippine Sea over the last one million years. Palaeogeogr. Palaeoclimatol. Palaeoecol. 326, 152–159.
Wang, Y.J., Cheng, H., Edwards, R.L., An, Z., Wu, J., Shen, C., Dorale, J.A., 2001. A high-resolution absolute-dated Late Pleistocene monsoon record from Hulu Cave, China. Science 294, 2345–2348.
Wang, Y.J., Cheng, H., Edwards, R.L., Kong, X., Shao, X., Chen, S., Wu, J., Jiang, X., Wang, X., An, Z., 2008. Millennial- and orbital-scale changes in the East Asian monsoon over the past 224,000 years. Nature 451, 1090–1093.
Weber II, E.T., Owen, R.M., Dickens, G.R., Rea, D.K., 1998. Causes and implications of the middle rare earth element depletion in the eolian component of North Pacific sediment. Geochem. Cosmochim. Acta 62, 1735–1744.
Wei, G., Li, X.-H., Liu, Y., Shao, L., Liang, X., 2006. Geochemical record of chemical weathering and monsoon climate change since the early Miocene in the South China Sea. Paleoceanography 21, PA4214. https://doi.org/10.1029/2006PA001300.
West, A.J., 2012. Thickness of the chemical weathering zone and implications for erosional and climatic drivers of weathering and for carbon-cycle feedbacks. Geology 40, 811–814.
West, A.J., Galy, A., Bickle, M., 2005. Tectonic and climatic controls on silicate weathering. Earth Planet Sci. Lett. 235, 211–228.
White, A.F., Blum, A.E., 1995. Effects of climate on chemical weathering in watersheds. Geochem. Cosmochim. Acta 59, 1729–1747.
Wodzicki, K.R., Rapp, A.D., 2016. Long-term characterization of the Pacific ITCZ using TRMM, GPCP, and ERA-Interim. J. Geophys. Res.: Atmosphere 121, 3153–3170.
Wu, G., Zhang, C., Zhang, X., Tian, L., Yao, T., 2010. Sr and Nd isotopic composition of dust in Dunde ice core, Northern China: implications for source tracing and use as an analogue of long-range transported Asian dust. Earth Planet Sci. Lett. 299, 409–416.
Wu, R., Hu, Z.-Z., Kirtman, B.P., 2003. Evolution of ENSO-related rainfall anomalies in east Asia. J. Clim. 16, 3742–3758.
Xiong, Z., Li, T., Algeo, T., Chang, F., Yin, X., Xu, Z., 2012a. Rare earth element geochemistry of laminated diatom mats from tropical West Pacific: evidence for more reducing bottomwaters and higher primary productivity during the Last Glacial Maximum. Chem. Geol. 296–297, 103–118.
Xiong, Z., Li, T., Algeo, T., Nan, Q., Zhai, B., Lu, B., 2012b. Paleoproductivity and paleoredox conditions during late Pleistocene accumulation of laminated diatom mats in the tropical West Pacific. Chem. Geol. 334, 77–91.
Xiong, Z., Li, T., Algeo, T., Doering, K., Frank, M., Brzezinski, M.A., Chang, F., Opfergelt, S., Crosta, X., Jiang, F., Wan, S., Zhai, B., 2015. The silicon isotope composition of Ethmodiscus rex laminated diatom mats from the tropical West Pacific: implications for silicate cycling during the Last Glacial Maximum. Paleoceanography 30, 803–823.
Xiong, Z., Li, T., Chang, F., Algeo, T., Clift, P., Bretschneider, L., Lu, Z., Zhu, X., Frank, M., Sauer, P., Jiang, F., Wan, S., Zhang, X., Chen, S., Huang, J., 2018. Data for: Rapid precipitation changes in the tropical West Pacific linked to North Atlantic climate forcing during the last deglaciation. Mendeley Data 1. https://doi.org/10.17632/t2y8s77ghp.1.
Xu, Z., Li, T., Wan, S., Nan, Q., Li, A., Chang, F., Jiang, F., Tang, Z., 2012. Evolution of East Asian monsoon: clay mineral evidence in the western Philippine Sea over the past 700 kyr. J. Asian Earth Sci. 60, 188–196.
Xu, Z., Li, T., Yu, X., Li, A., Tang, Z., Choi, J., Nan, Q., 2013. Sediment provenance and evolution of the East Asian winter monsoon since 700 ka recorded by major elements in the West Philippine Sea. Chin. Sci. Bull. 58, 1–9.
Xu, Z., Li, T., Clift, P.D., Lim, D., Wan, S., Chen, H., Tang, Z., Jiang, F., Xiong, Z., 2015. Quantitative estimates of Asian dust input to the western Philippine Sea in the mid-late Quaternary and its potential significance for paleoenvironment. G-cubed 16, 3182–3196.
Yan, H., Wei, W., Soon, W., An, Z., Zhou, W., Liu, Z., Wang, Y., Carter, R.M., 2015. Dynamics of the intertropical convergence zone over the western Pacific during the Little ice age. Nat. Geosci. 8, 315–320.
Yokoyama, Y., Lambeck, K., De Deckker, P., Johnston, P., Fifield, L.K., 2000. Timing of the Last Glacial Maximum from observed Sea-level minima. Nature 406, 713–716.
Zhang, Y., Chiessi, C.M., Mulitza, S., Zabel, M., Trindade, R.I.F., Hollanda, M.H., Dantas, E.L., Govin, A., Tiedemann, R., Wefer, G., 2015. Origin of increased terrigenous supply to the NE south American continental margin during Heinrich stadial 1 and the younger Dryas. Earth Planet Sci. Lett. 432, 493–500.